Journal of Materials Chemistry A

ROYAL SOCIETY OF CHEMISTRY

PAPER

View Article Online
View Journal

Cite this: DOI: 10.1039/d0ta06348g

High-performance solid-state hybrid supercapacitor enabled by metal–organic framework-derived multi-component hybrid electrodes of Co–N–C nanofibers and $Co_{2-x}Fe_xP$–N–C micropillars†

Thangjam Ibomcha Singh, [ab] G. Rajeshkhanna,[c] Tolendra Kshetri, [a] Nam Hoon Kim *[a] and Joong Hee Lee *[ad]

In recent years, much effort has been devoted to developing hybrid supercapacitors due to their capability to deliver both high energy and power density. The hybrid approach is advantageous in terms of reinforcing the synergic combination of the properties of different components in a hybrid composite. However, a large kinetic mismatch existing between the fast capacitive and sluggish battery-type electrodes greatly hinders its advancement. In this work, we report the fabrication of a solid-state hybrid supercapacitor (SSHSC) device using metal–organic framework (MOF)-derived cobalt-embedded N-doped carbon nanofibers (Co–N-CNFs) and $Co_{2-x}Fe_xP$–N–C micropillar arrays grown on Ni foam ($Co_{2-x}Fe_xP$–N–C/NF) as multi-component hybrid electrodes with improved charge storage kinetics. Such Co–N-CNFs (negative electrode) exhibited a remarkable specific capacitance of 280 F g^{-1} at a current density of 1 A g^{-1}, while $Co_{2-x}Fe_xP$–N–C/NF (positive electrode) exhibited a high specific capacity of 345 mA h g^{-1} at a current density of 1 A g^{-1} due to the synergistic combinations of different components in a single hybrid composite. The assembled $Co_{2-x}Fe_xP$–N–C/NF(+)//Co–N-CNFs(–) SSHSC device demonstrated a high specific capacity of 104 mA h g^{-1} at a current density of 1 A g^{-1} with a maximum energy density of 84.7 W h kg^{-1} at a power density of 706 W kg^{-1}. It also exhibited excellent stability and reversibility with a capacity retention of 93% and coulombic efficiency of 99.6% after 10 000 galvanostatic charge–discharge (GCD) cycles. Two SSHSC devices connected in series after being charged could easily light up a red LED bulb. These excellent performances indicate that Co–N-CNFs(–) and $Co_{2-x}Fe_xP$–N–C/NF(+) materials could be considered as potential electrodes for high energy density storage systems.

Received 29th June 2020
Accepted 22nd November 2020

DOI: 10.1039/d0ta06348g

rsc.li/materials-a

1. Introduction

In the rapidly growing science and technological fields, energy storage devices such as supercapacitors (SCs) and batteries are in great demand for various applications ranging from small scale portable electronic gadgets to large scale hybrid electric vehicles.[1,2] Over the last two decades, researchers have been largely attracted towards SCs because of their high power density, fast charge/discharge rate capability, and long cycle life as compared to batteries.[1–5] Currently, SCs are replacing batteries in some applications where high power density is required. However, the energy density of SCs is worse than that of batteries.[3,6,7] To improve their energy densities, hybrid supercapacitors have been developed by combining non-faradaic carbon-based materials and faradaic battery-type materials as composites and asymmetric combinations.[6,7] A hybrid supercapacitor consisting of a non-faradaic capacitive material as a negative electrode and a faradaic battery-type material as a positive electrode exhibits both high power density and high energy density.[6,7] Nevertheless, the development of a hybrid supercapacitor is greatly hindered due to the large kinetic mismatch between the fast reaction kinetics of carbon-based capacitive electrodes and relatively slow reaction kinetics of counter faradaic battery-type electrodes.[3,6,7] Such a kinetic discrepancy has a negative influence on the performance of hybrid supercapacitors.[6] So far, hybrid

[a]Department of Nano Convergence Engineering, Jeonbuk National University, Jeonju, Jeonbuk, 54896, Republic of Korea. E-mail: nhk@jbnu.ac.kr; jhl@jbnu.ac.kr
[b]Faculty of Science, Engineering & Technology, Swinburne University of Technology, PO Box 218, Hawthorn, VIC 3122, Australia
[c]Department of Chemistry, National Institute of Technology, Warangal, India
[d]Center for Carbon Composite Materials, Department of Polymer-Nano Science and Technology, Jeonbuk National University, Jeonju, Jeonbuk, 54896, Republic of Korea

† Electronic supplementary information (ESI) available: Digital photographs, XRD, FE-SEM, EDS spectra, optimization of ZIF-67 : PAN ratio, additional electrochemical characterizations, table for comparison of the electrochemical performance of the negative electrode, positive electrode and solid-state hybrid supercapacitor. See DOI: 10.1039/d0ta06348g

supercapacitors have been fabricated using pure carbon-based materials such as activated carbon (AC), graphene carbon nanotubes (CNTs), carbon nanofibers (CNFs), and so on as negative electrodes,[8–11] and transition metal (TM)-based materials such as oxides, hydroxides, sulfides, and so on as battery-type positive electrodes.[12–14] These materials used in hybrid supercapacitors have several drawbacks such as the low capacitance of pure carbon materials and low electrical conductivity of TM-based materials.[8,15]

To avoid the limitations mentioned above, a suitable design of electrode materials in terms of elemental composition, morphology, and structure that can lead to minimal kinetic difference, high capacitance, and high conductivity is urgently needed. In addition, parameters such as specific surface area (SSA), porosity, and morphology have to be optimized to augment the overall charge storage performance.[16,17] Introducing a faradaic component in carbon electrodes (electrical double-layer capacitance, *viz.* EDLC) and an EDLC component in the faradaic battery-type electrode can minimize the kinetic difference and enhance the capacitance of the carbon electrode and conductivity of the faradaic electrode.[6,7] In this regard, metal–organic frameworks (MOFs) consisting of periodic networks of metal ions and organic ligands can be great precursors for deriving electrode materials with unique elemental compositions and morphology that exhibit interesting physicochemical properties.[18–21] For instance, N-doped porous carbon materials derived from ZIF-8 in inert atmospheres showed an SSA of 720 $m^2\ g^{-1}$ and capacitance of 130 F g^{-1} at 50 mV s^{-1}.[22] Recent reports have also shown that TM phosphides are promising materials for energy storage applications due to their higher electrical conductivity and better metalloid characteristics than oxides and hydroxides.[23–26] Very recently, Lan *et al.* have reported that NiCoP@NF nanosheets have a high capacitance of 2143 F g^{-1} at a current density of 1 A g^{-1}.[24] Interestingly, during the conversion of the MOF precursor to metal phosphide at its decomposition temperature in an inert atmosphere, traces of N-doped carbons (N–C) are produced owing to the nitrogen-containing organic ligand.[27,28] These metal phosphides/N–C compositions are expected to show relatively higher charge storage kinetics and conductivity due to the presence of N–C. Therefore, a hybrid supercapacitor made of MOF derived TM phosphides/N–C materials and another MOF derived Co-embedded N–C material as positive and negative electrodes, respectively, can significantly boost the energy density.

Considering the above-mentioned aspects, in this work, we successfully synthesized a necklace-like Co-embedded N–C nanofiber (Co–N-CNFs) *via* electrospinning with subsequent carbonization of polyacrylonitrile (PAN) and ZIF-67 nanofiber composite network as a negative electrode material. On the other hand, mesoporous $Co_{2-x}Fe_xP$–N–C micropillar arrays on a Ni foam substrate derived from the corresponding metal–organic framework known to be a Prussian blue analogue (CoFe-PBA) *via* phosphorization was used as a positive electrode material. During the synthesis, $Co_{2-x}Fe_xP$–N–C micropillar arrays were *in situ* grown on a Ni foam substrate, which acted as a current collector, thus avoiding the necessity of using an inactive polymer as a binder for electrode preparation. This led to more exposure of electrochemically active surface area (ECSA) and improved conductivity, thereby enhancing both energy storage capability and stability. The electrospinning process enabled the interconnection between individual units of ZIF-67 using PAN nanofibers. The resulting Co-embedded N–C nanofiber provided an efficient pathway for transporting electron and electrolyte ions during charging–discharging processes. When charge storage performances of Co-embedded N–C nanofibers (Co–N-CNFs) and $Co_{2-x}Fe_xP$–N–C materials were evaluated with a three-electrode system, they exhibited high specific capacitance/capacity values and robust cycling stability. Using Co–N-CNFs as a negative electrode, $Co_{2-x}Fe_xP$–N–C as a positive electrode, and PVA/KOH gel as an electrolyte, a solid-state hybrid supercapacitor (SSHSC) was fabricated. Such an SSHSC demonstrated high specific capacity and high energy density at high power density with exceptional cycling stability and coulombic efficiency due to synergistic effects resulting from its unique compositions and physicochemical properties.

2. Experimental section

Chemicals used in this study included polyacrylonitrile (PAN, average M_w = 150 000 supplied by Aldrich), cobalt chloride hexahydrate ($CoCl_2 \cdot 6H_2O$), potassium hexacyanoferrate ($K_3[Fe(CN)_6]$), cobalt nitrate hexahydrate ($Co(NO_3)_2 \cdot 6H_2O$), 2-methylimidazole, methanol, *N*,*N*-dimethylformamide (DMF), DI water, polyvinylpyrrolidone (PVP), cellulose filter paper NKK TF40 (thickness of 40 μm), polyvinyl alcohol (PVA), potassium hydroxide (KOH), and Ni foam (NF) (99.9% Ni percentage, 98% porosity, 0.2–0.5 mm pore size, thickness ~ 1.5 mm, density ~ 380 g m^2 ± 20, length 250 mm) obtained from Taiyuan Liyuan Lithium Technology Co. Ltd, China.

2.1 Synthesis of electrospun Co-embedded N–C nanofibers (Co–N-CNFs) (negative electrode material)

2.1.1 Synthesis of ZIF-67. Initially, ZIF-67 was synthesized as described previously with a slight modification.[29] In a typical synthesis, two solutions were prepared separately. First, 520 mg of cobalt chloride hexahydrate ($CoCl_2 \cdot 6H_2O$) and 600 mg of polyvinylpyrrolidone (PVP) were dissolved in 40 mL of methanol in one beaker. In another beaker, 2.63 g of 2-methylimidazole was dissolved in 40 mL of methanol. Finally, these two solutions were then slowly mixed under magnetic stirring at 300 rpm for 5 min at room temperature (25 °C). Magnetic stirring was then stopped, and the mixture was allowed to age for 24 h. The resultant precipitate was collected by centrifugation at 9000 rpm for 10 min, washed five times with methanol, and dried in a conventional electric oven at 60 °C for 10 h.

2.1.2 Synthesis of electrospun PAN-ZIF-67 nanofibers (EPZ-67-NFs). In a typical synthesis, an electrospinning solution was prepared by dissolving 1.5 g of PAN in 13.5 g of DMF solvent in a 50 mL vial under constant magnetic stirring at 60 °C. To this solution, as-prepared ZIF-67 was added. To optimize the loading of ZIF-67, different proportions of ZIF-67 (ZIF-67 to PAN ratio of 1 : 10, 1 : 5, 1 : 3, and 1 : 2.5) were added followed by

continued stirring for 12 h. Each resultant solution was loaded into a 12 mL plastic syringe connected to a plastic nozzle. It was then electrospun using an electrospinning machine (BFT-ES1000, FGM) at an applied voltage of 12.6 kV. The distance between the tip of the nozzle and the collector was fixed at 150 mm. The flow rate was set at 650 μL h^{-1}. The temperature and humidity were fixed at 25 °C and 30% throughout the entire electrospinning process. An aluminum foil wrapped metallic drum, which was grounded electrically, acted as a nanofiber collector. The rotation speed of the drum was maintained at 400 rpm for 8 h. Finally, electrospun PAN-ZIF-67 nanofibers (EPZ-67-NFs) were collected by removing the aluminum foil from the drum collector. They were then pressed using hydraulic pressure (39 kPa) to obtain free-standing electrospun PAN-ZIF-67 nanofiber (EPZ-67-NF) mats. Electrospun PAN-ZIF-67 nanofiber prepared with a ZIF-67 to PAN ratio of 1 : 3 was considered as the optimum sample due to better uniform distribution of ZIF-67 in the PAN nanofiber. Increasing ZIF-67 loading to a ratio of more than 1 : 3 caused difficulty in the electrospinning process. For comparison, electrospun pristine PAN nanofibers (EP-NFs) without ZIF-67 were also prepared under similar electrospinning conditions.

2.1.3 Synthesis of Co-embedded N-doped carbon nanofibers (Co–N-CNFs). As-prepared electrospun EPZ-67-NFs were cut into small pieces (2 × 4 cm^2 in area) and put in a crucible, which was then placed inside a furnace. The furnace was heated to 550 °C with a ramping rate of 2 °C min^{-1} in an Ar atmosphere. It was then held at 550 °C for 1 h. The temperature was then increased to 800 °C with a ramping rate of 5 °C min^{-1}. The temperature was then maintained at 800 °C for 2 h in the Ar atmosphere to finally obtain Co-embedded N–C nanofibers (Co–N-CNFs). For comparison, pristine electrospun PAN nanofiber (EP-NF) was also carbonized under similar conditions to obtain electrospun PAN derived N-doped carbon nanofiber denoted as N-CNF. For the comparative electrochemical study, Co–N-CNFs prepared from the optimized precursor sample were subjected to acid washing with 3 M HCl solution for 10 h at 60 °C under slow magnetic stirring. They were then washed several times with DI water till the pH became 7. They were then dried in a conventional oven at 60 °C for 12 h.

2.2 Synthesis of $Co_{2-x}Fe_xP$–N–C/NF (positive electrode material)

The $Co_{2-x}Fe_xP$–N–C/NF electrode was synthesized similar to our previous report with a slight modification.[27]

2.2.1 Synthesis of Co-MOF/NF. First, 1 mmol of cobalt nitrate hexahydrate and 16 mmol of 2-methylimidazole were separately dissolved in 40 mL of DI water. They were then mixed together under magnetic stirring for 1 min. Two pieces of pre-cleaned Ni foam (2 × 4 cm^2 in area) were placed into the solution and aged for 12 h. Under these conditions, Co-MOF was uniformly grown on Ni foam (Co-MOF/NF). Co-MOF grown Ni foam pieces were collected, washed with DI water, and dried in an oven at 60 °C for 12 h.

2.2.2 Synthesis of CoFe-PBA/NF. Two pieces of as-prepared Co-MOF/NF (2 × 4 cm^2) were immersed in 0.01 M aqueous solution of potassium hexacyanoferrate ($K_3[Fe(CN)_6]$) in a beaker for 12 h at room temperature (25 °C). After that, they were collected, washed with DI water and dried at 60 °C for 12 h.

2.2.3 Synthesis of $Co_{2-x}Fe_xP$–N–C/NF. The synthesized CoFe-PBA/NF was converted to $Co_{2-x}Fe_xP$–N–C/NF using a solid–gas phosphorization technique. For this conversion process, a quartz boat containing 1 g of sodium hypophosphide was placed in a quartz boat inside a furnace tube 2 cm ahead of another boat containing a piece of CoFe-PBA/NF. The temperature was initially raised to 400 °C at a very slow heating rate of 1 °C min^{-1} in an Ar atmosphere. This temperature was then maintained for 2 h in the same atmosphere throughout the process, after which it was cooled down to room temperature. For comparison, Co-MOF/NF was also converted to Co_2P–N–C/NF under similar heating conditions.

2.3 Electrochemical characterization

To evaluate the charge storage capability of each synthesized material, cyclic voltammetry (CV), galvanostatic charge discharge (GCD), and electrochemical impedance spectroscopy (EIS) techniques were employed in both three-electrode and two-electrode configurations using a CHI 660E electrochemical workstation (CHI, USA).

In the three-electrode system, 1 × 1 cm^2 area of Co–N-CNFs (mass loading = 3 mg) and 1 × 1 cm^2 area of $Co_{2-x}Fe_xP$–N–C/NF (mass loading = 2 mg) were used as the working electrode, while Pt foil (1 × 1 cm^2) and Hg/HgO were used as counter and reference electrodes, respectively. The N-CNF and Co–N-CNF materials were all sandwiched between two pre-cleaned Ni foams acting as the current collector, using hydraulic pressure (Carver Hydraulic unit model #3912, USA), similar to previous reports.[11,30] A freshly prepared 6 M KOH aqueous solution was employed as the electrolyte. EIS measurements were performed at open circuit potentials (OCPs) with a frequency range of 0.01 to 10^5 Hz and voltage amplitude of 5 mV. Before taking electrochemical measurements, working electrode materials were stabilized with 100 continuous CV cycles at a scan rate of 20 mV s^{-1}.

For the two electrode system, a hybrid supercapacitor was constructed using a Split test cell (MTI Cooperation, USA). For constructing a hybrid supercapacitor, Co–N-CNFs and $Co_{2-x}Fe_xP$–N–C/NF were used as negative and positive electrodes, respectively, with a cellulose filter paper NKK TF40 (thickness of 40 μm) as the separator and PVA/KOH gel as the electrolyte. Initially, PVA/KOH gel electrolyte was prepared by dissolving 3 g of PVA and 2 g of KOH in 36 mL DI water at 90 °C with magnetic stirring for 1 h, similar to our previous report.[14] The separator was then dipped into the gel electrolyte, and the solid-state hybrid supercapacitor (SSHSC) was finally fabricated by inserting a PVA/KOH gel coated separator between the electrodes.

For the optimum electrochemical performance of the device, the mass ratio of electrode materials was calculated using the following charge balance eqn (1),[31]

$$\frac{m_+}{m_-} = \frac{C_- \times V_-}{C_+ \times V_+} \quad (1)$$

where m_+, C_+, and V_+ are the mass, capacitance, and potential window of the positive electrode materials, respectively. m_-, C_-, and V_- are the mass, capacitance, and potential window of the negative electrode materials, respectively. The optimised mass ratio of the $Co_{2-x}Fe_xP$–N–C/NF positive electrode and Co–N-CNF negative electrode used in the fabrication of the hybrid device as calculated using eqn (1) was 1 : 2.

The galvanostatic charge–discharge (GCD) specific capacitance value (C_{sc}, F g^{-1}), the voltammetric specific capacitance (C_{vs}, F g^{-1}) of the negative electrode and the specific capacity (C_s, mA h g^{-1}) of the positive electrode were calculated using eqn (2), (3) and (4), respectively.[14,32]

$$C_{sc} = \frac{2I\int U\mathrm{d}t}{m(\Delta U)^2} \quad (2)$$

$$C_{vs} = \frac{\int I\mathrm{d}U}{m\nu\Delta U} \quad (3)$$

$$C_s = \frac{2I \times \int U\mathrm{d}t}{m\Delta U} \quad (4)$$

where I is the current applied (A), $\int U\mathrm{d}t$ is the integral area under the GCD discharge curve, $\int I\mathrm{d}U$ is the voltammetric charge (area under the CV curve), ν is the scan rate (mV s^{-1}), m is the mass of the electrode material (positive/negative) (g), and ΔU is the working potential window range (V).[32]

Electrochemically active surface area (ECSA) was calculated using eqn (5),[33]

$$\mathrm{ECSA} = \frac{C_{dl}}{C_s} \quad (5)$$

where C_{dl} is the capacitance calculated from the non-faradaic region and C_s is the capacitance of a flat smooth electrode surface, numerically taken as 40 μF cm^{-2}.[33] For the calculation of C_{dl}, cyclic voltammograms of the electrode material were recorded in the non-faradaic region at various scan rates. A graph of scan rates *versus* current densities ($\Delta j = j_{anodic} - j_{cathodic}$) was plotted, and the slope of the graph was determined through linear fitting. The estimated slope is numerically equal to twice the C_{dl} value. Hence, the C_{dl} value would be half of the slope value.

The specific capacity (C_{scell}, mA h g^{-1}), coulombic efficiency (η), energy density (E_{cell}), and power density (P_{cell}) of the SSHSC were calculated using eqn (6), (7), (8), and (9), respectively.[14]

$$C_{s,cell} = \frac{2I_{cell} \times \int U\mathrm{d}t}{m_{cell} \times U_{cell}} \quad (6)$$

$$\eta = \frac{t^d_{cell}}{t^c_{cell}} \quad (7)$$

$$E_{cell} = \frac{I_{cell} \times \int U\mathrm{d}t}{m_{cell} \times 3.6} \quad (8)$$

$$P_{cell} = \frac{E_{cell} \times 3600}{t^d_{cell}} \quad (9)$$

where I_{cell} is the current of the device, m_{cell} is the total mass of the electrode materials in the device (mass of both positive and negative electrode materials), $\int U\mathrm{d}t$ is the area under the discharge curve, and t^d_{cell} and t^c_{cell} are the discharge and charge times of the hybrid device.

2.4 Physical characterization methods

The crystallinity and phase of each prepared material were investigated by powder X-ray diffraction (P-XRD) (Rigaku Corporation, Japan, CuKα radiation, wavelength = 0.154 nm) in the 2θ range of 10–80° at a scan rate of 3° min^{-1}. Surface morphology, internal structure, and elemental compositions were examined using field emission scanning electron microscopy (FE-SEM) (JSM-6701F; JEOL, Japan), transmission electron microscopy (TEM) (JEM-2200 FS, JEOL Ltd, Japan, 200 kV), and energy-dispersive X-ray spectroscopy (EDS) (SUPRA 40 VP, Carl Zeiss, Germany) a the Centre for University-Wide Research Facilities (CURF) in Jeonbuk National University. Near-surface chemical compositions and valence states of elements were investigated by X-ray photoelectron spectroscopy (XPS) (Theta Probe; Thermo Fisher Scientific, UK) in the Jeonju Center of the KBSI. The multipoint nitrogen adsorption–desorption experiment was performed with an ASAP 2020 Plus Accelerated Surface Area and Porosimetry System (Micromeritics Instrument Corp., USA) after degassing all the samples at 100 °C for 15 h with the help of a dynamic vacuum. Specific surface areas (SSA) and pore size distributions of the materials were evaluated using Brunauer–Emmett–Teller (BET) and Barrett–Joyner–Halenda (BJH) methods, respectively, at 77 K. The sheet resistances of the prepared N-CNFs and Co–N-CNFs were determined using a four-point-probe surface resistivity meter (MSTEC) coupled with a Keithley-2182A nano-voltmeter having a Keithley-6221 DC/AC as a current source. The wettability of N-CNFs and Co–N-CNFs was evaluated by measuring their contact angles with DI water using a drop shape analyser-DSA30, Kruss.

3. Results and discussion

Fig. 1 shows the detailed synthesis scheme of Co-embedded N-doped carbon nanofibers (Co–N-CNFs) and $Co_{2-x}Fe_xP$–N–C/NF materials. The negative electrode material Co–N-CNFs was synthesized *via* a combined electrospinning with a subsequent carbonization technique (a), while the positive electrode material $Co_{2-x}Fe_xP$–N–C/NF was obtained through a solid–gas phosphorization technique (b). The development of the Co–N-CNF material is photographically shown in Fig. S1 of the ESI.†

3.1 Physical characterization

Fig. 2a and b show PXRD patterns of as-prepared ZIF-67 particles, electrospun PAN (EP-NFs), and electrospun PAN-ZIF-67 nanofibers (EPZ-67-NFs) before and after carbonization. The diffraction pattern of ZIF-67 showed dominant peaks at 2θ values of 7.32°, 10.36°, 12.69°, 14.63°, 16.37°, and 18° corresponding to (011), (002), (112), (022), (013), and (222) planes, respectively, confirming the formation of orthorhombic ZIF-67. These results were consistent with the results of the previous

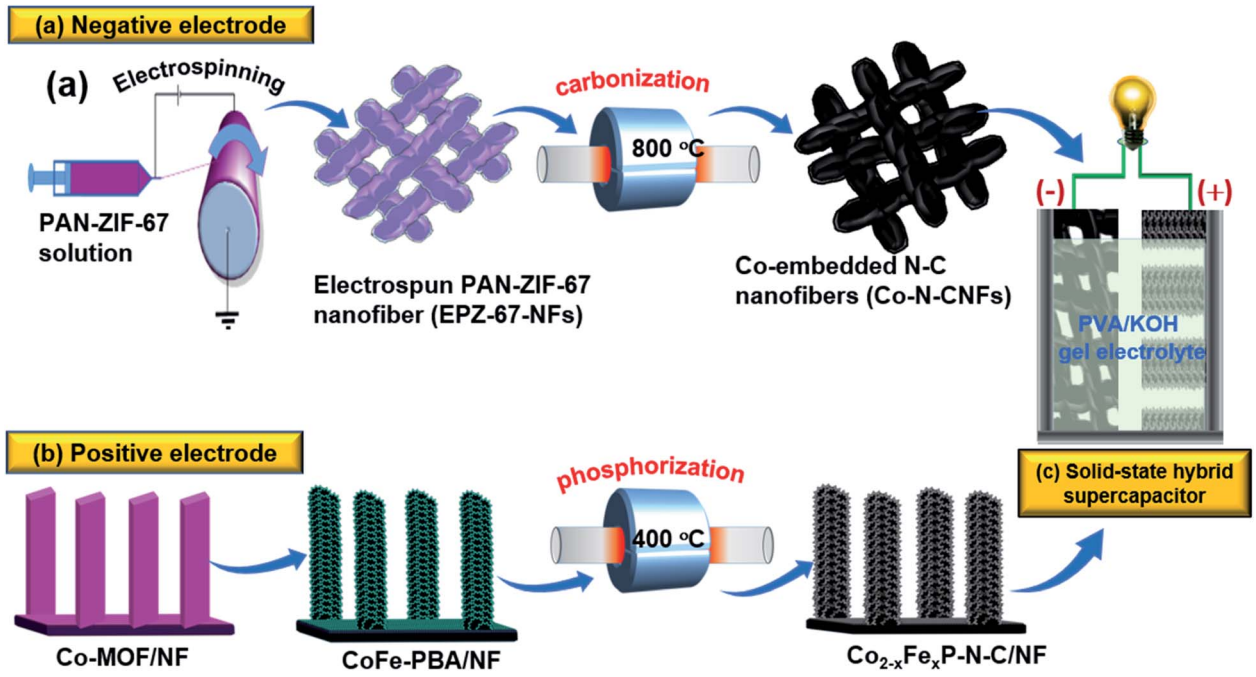

Fig. 1 Schematic illustration for the synthesis of (a) cobalt-embedded nitrogen doped carbon nanofibers (Co–N-CNFs), (b) $Co_{2-x}Fe_xP$–N–C micropillar arrays on Ni foam ($Co_{2-x}Fe_xP$–N–C/NF), and (c) fabrication of a solid-state hybrid supercapacitor (SSHSC) using Co–N-CNFs and $Co_{2-x}Fe_xP$–N–C/NF as negative and positive electrodes, respectively, with PVA/KOH gel as the electrolyte.

report.[34] These peaks were also observed for EPZ-67-NFs, indicating that the ZIF-67 phase remained unchanged even after electrospinning. After carbonization at 800 °C in an Ar atmosphere, corresponding diffraction patterns were changed to their derivative diffraction patterns (Fig. 2b). All these three materials showed a broad peak between 2θ values of *ca.* 20° and 30° (Fig. 2b) corresponding to the carbon (C) (002) plane, indicating that all three materials were carbonized.[22,35] However, the carbon (002) plane of these three materials (Co–N–C, N–C, Co–N-CNFs) appeared at different positions in their PXRD patterns. This might be attributed to lattice compression or relaxation resulting from their corresponding precursor materials.[35] Carbonized ZIF-67 (Co–N–C), and EPZ-67-NFs (Co–N-CNFs) materials showed high intense peaks at 2θ values of 44.4°, 51.5°, and 76.1° corresponding to metallic cobalt (JCPDS-ICCD: 96-901-0969) resulting from Co-metal sites in the ZIF-67 framework.[17,35] The formation of metallic Co nanoparticles in the carbon nanofiber network can improve the overall electrical conductivity, wettability, and charge storage ability of the Co–N-CNF electrode.[17,35,36] Fig. 2c shows PXRD patterns of pristine Co_2P–N–C/NF and $Co_{2-x}Fe_xP$–N–C/NF derived from Co-MOF/NF and CoFe-PBA/NF, respectively. The PXRD of the Co_2P–N–C/NF material showed peaks at 27.08°, 31.16°, 32.82°, 40.64°, 43.25°, 48.70°, and 56.10° consistent with Co_2P (JCPDS-ICCD: 32-0306). The PXRD pattern of $Co_{2-x}Fe_xP$–N–C/NF (Fig. 2c) showed peaks at 26.80°, 30.41°, 32.82°, 35.30°, 40.70°, 47.12°, 48.88°, 52.92°, and 54.06°. These peak positions were almost identical to binary metal phosphides of Co_2P (JCPDS: 32-0306) and Fe_2P (JCPDS: 85-1727), indicating the existence of mixed phases.[27] Highly intense peaks at 2θ values of 44.10°, 51.12°, and 76.23° were Ni peaks from the Ni foam substrate. PXRD patterns of Co-MOF/NF and CoFe-PBA/NF precursor materials are also shown in Fig. S2, ESI.† Their peaks were consistent with previous reports.[27,37] Thus, PXRD analyses revealed the formation of the respective phases of the prepared materials.

The degree of graphitization and the local environment of Co–N-CNFs were investigated using Raman spectroscopy. Corresponding spectra are presented in Fig. 2d. The Raman spectrum of Co–N-CNFs showed two main peaks at 1352 cm^{-1} and 1575 cm^{-1} corresponding to the D-band (defects) and G-band (graphitic), respectively.[22,35,38] The D-band arises from sp^3 bonded carbon atoms known to have disordered or defective structures, while the G-band is attributed to the graphitic carbon layers.[22,35,38] The ratio of the intensity of the D-band to that of the G-band (I_D/I_G) for Co–N-CNFs was about 1, which was higher than that of electrospun PAN derived N-CNFs (I_D/I_G = 0.85). Such an increase in the I_D/I_G ratio of Co–N-CNFs compared to N-CNFs can be attributed to increased structural defects induced by the inclusion of ZIF-67 nanoparticles in Co–N-CNFs.[35,38]

Specific surface area (SSA) and pore size distribution of Co–N-CNFs and $Co_{2-x}Fe_xP$–N–C/NF electrode materials were estimated from N_2 adsorption–desorption isotherms using Brunauer–Emmett–Teller (BET) and Barret–Joyner–Halenda (BJH) methods (Fig. 2e and f). Isotherms of Co–N-CNFs and $Co_{2-x}Fe_xP$–N–C/NF materials were similar to a typical Type-IV isotherm curve with an H-4 hysteresis loop, indicating the presence of hierarchical mesopores.[39] The estimated SSA of Co–N-CNFs was 215.86 $m^2\ g^{-1}$, which is about 7 times more than the SSA of N-CNFs (29.26 $m^2\ g^{-1}$). There was a sharp N_2 uptake

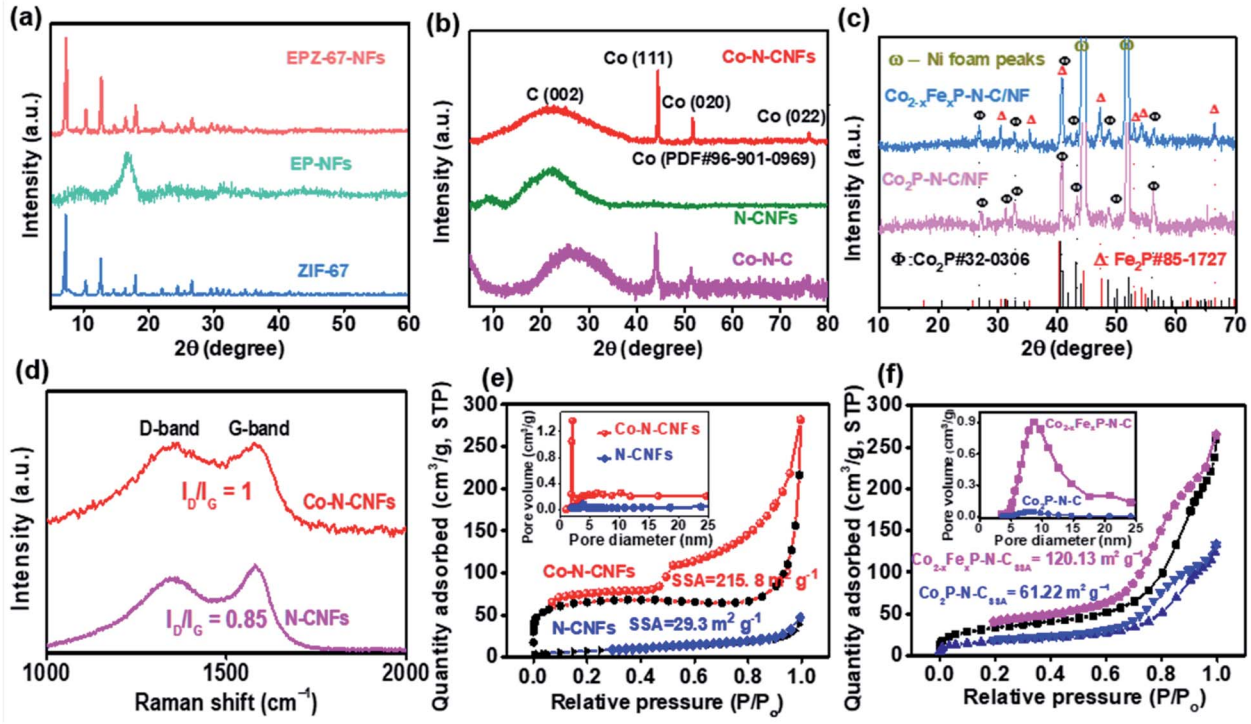

Fig. 2 (a–c) PXRD patterns of (a) ZIF-67, electrospun PAN nanofiber (EP-NFs), PAN-ZIF-67 nanofibers (EPZ-67-NFs), (b) Co–N–C, N-CNFs and Co–N-CNFs, obtained after the carbonization of ZIF-67, EP-NFs and EPZ-67-NFs, respectively, and (c) pristine Co_2P–N–C/NF and $Co_{2-x}Fe_xP$–N–C/NF; (d) Raman spectra of N-CNFs and Co–N-CNFs; (e) N_2 adsorption–desorption isotherm profile of Co–N-CNFs in comparison with that of N-CNFs, (f) N_2 adsorption–desorption isotherm profile of $Co_{2-x}Fe_xP$–N–C in comparison with that of Co_2P–N–C, insets of (e) and (f) show corresponding BJH pore size distribution profiles.

at a very low relative pressure (P/P_o) within the range of ~0 to ~0.05 due to the existence of abundant micropores.[40] A sharp increase in the N_2 adsorption in the range of 0.9–1.0 indicated the presence of macropores.[39,40] BJH pore size distribution (inset of Fig. 2e) further supported the existence of micropores. Previous studies have shown that micropores can significantly enhance the capacitance of carbon-based electrode materials due to nanoconfinement effects.[41,42] Therefore, Co–N-CNFs are expected to show high capacitance due to the presence of abundant micropores and their high SSA. Besides, the estimated SSA and pore volume of the $Co_{2-x}Fe_xP$–N–C positive electrode material were 118.41 $m^2\ g^{-1}$ and 0.34 $cm^3\ g^{-1}$, respectively. They were higher than those of single component Co-MOF/NF derived Co_2P–N–C/NF (61.22 $m^2\ g^{-1}$ and 0.20 $cm^3\ g^{-1}$, respectively). The BET isotherm (Fig. 2f) and BJH pore size distribution profile (inset of Fig. 2f) of $Co_{2-x}Fe_xP$–N–C showed the highly mesoporous nature of the $Co_{2-x}Fe_xP$–N–C material which was much uniform than Co_2P–N–C/NF (inset of Fig. 2f). Such high mesoporosity and large external surface area are advantageous in terms of shortening the charge transport paths as they allow free movement of electrolyte ions into electrode materials.[11]

A field-emission scanning electron microscope (FE-SEM) was used to examine the external surface morphologies of the synthesized materials. FE-SEM images of as-prepared ZIF-67 and pristine EP-NFs are shown in Fig. S3 and S4, ESI.† Low- and high-magnification FE-SEM images of ZIF-67 demonstrated uniform three dimensional (3D) orthorhombic structures with an average size of 2 μm (Fig. S3, ESI†), while FE-SEM images of EP-NFs showed interconnected and uniform nanofibers with high aspect ratios (Fig. S4, ESI†). The diameter of the nanofiber was *ca.* 300 nm (Fig. S4, ESI†). The morphology of ZIF-67 embedded PAN NFs resembled a necklace in which ZIF-67 particles acted as beads while the PAN polymer acts as the chain (Fig. S5, ESI†). FE-SEM images and EDS spectra of Co–N-CNFs prepared with different ZIF-67 : PAN ratios of 1 : 10, 1 : 5, and 1 : 3 shown in Fig. S6, ESI† also resembled a necklace. Uniform distribution of ZIF-67 particles in PAN NFs was achieved with a ZIF-67 : PAN ratio of 1 : 3 (Fig. S6c, ESI†). Further increase of ZIF-67 loading caused difficulty in the electrospinning process, consistent with a previous report.[43] Low- and high-magnification FE-SEM images of optimized EPZ-67-NFs derived Co–N-CNFs are shown in Fig. 3a–c. These images clearly showed that after converting into carbon, the structure was retained with high porosity (Fig. 3b and c). The combination of 3-D ZIF-67 particles with 1-D PAN nanofibers gave a unique multi-component nature to the Co–N-CNF material to show high conductivity and multi-functionalities, thereby promoting high charge storage capability.[44] As shown in Fig. 3b and c, there were small "Co" nanoparticles resulting from Co-metal sites of the ZIF-67 framework with the high porosity resulting from the decomposition of organic components during carbonization. The existence of metallic nanoparticles can improve electrical conductivity and surface wettability,

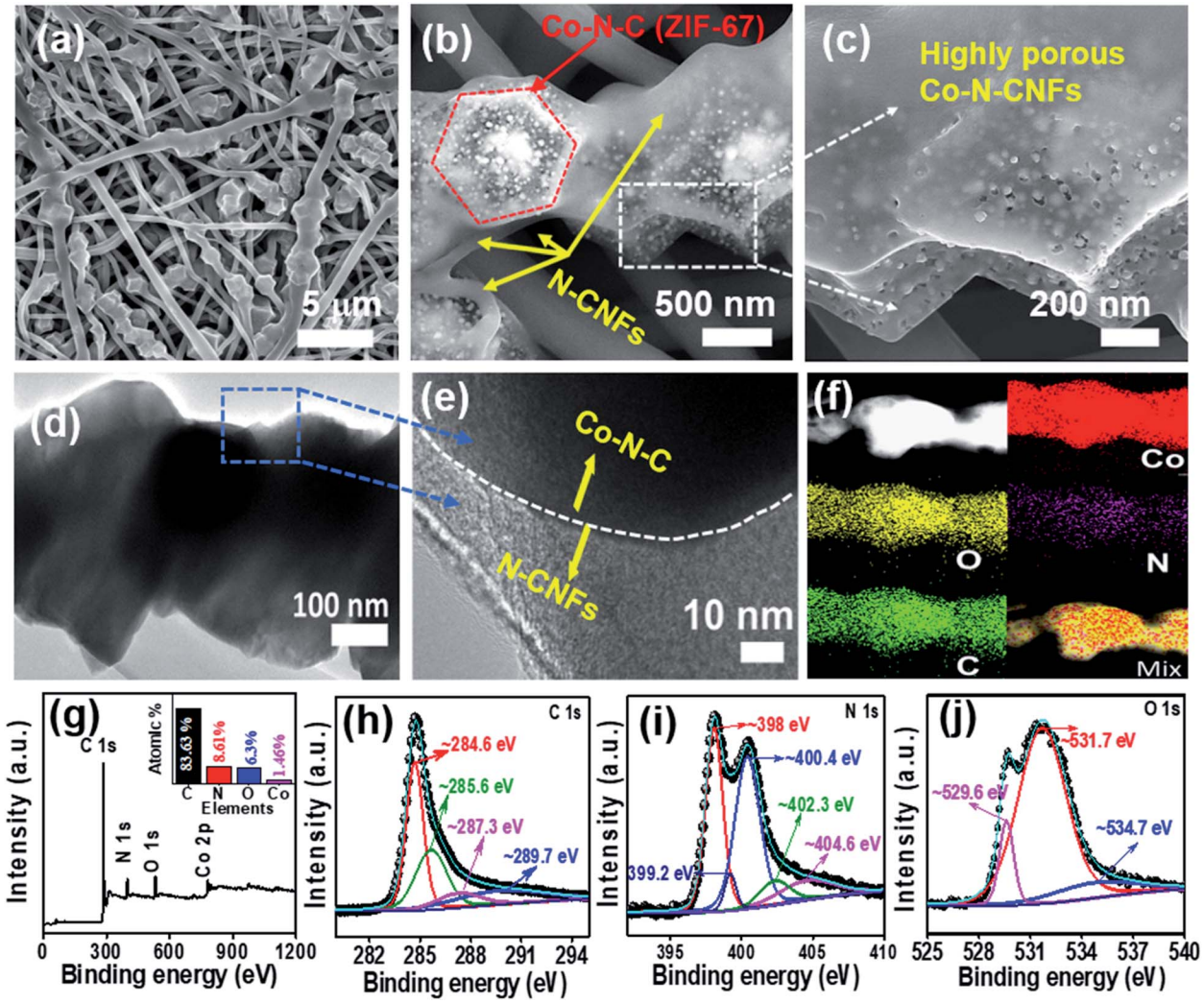

Fig. 3 (a–c) Low-and-high magnification FE-SEM images, (d and e) low- and high-magnification HR-TEM images, (f) HAADF-STEM image and EDS elemental color mapping images, (g) XPS survey spectrum with atomic percentages, (h) C 1s XPS spectrum, (i) N 1s XPS spectrum, and (j) O 1s XPS spectrum of Co–N-CNFs.

which can enhance electrode–electrolyte interaction and facilitate charge movements.[17,35] Co nanoparticles can also contribute to faradaic capacitance.[35] After the carbonization process, the optimized sample was washed in acid following the conventional strategy to create high porosity and large SSA from the morphological changes. FE-SEM images of the acid-washed material (denoted as Co–N-CNFs-acid wash) are shown in Fig. S7, ESI.† After acid washing, a large number of non-uniform macropores and fissures were formed on the surface of carbon nanofibers due to the removal of Co nanoparticles (Fig. S7b and c, ESI†). Although the SSA was enhanced from 215.86 $m^2 g^{-1}$ to 260.13 $m^2 g^{-1}$ after acid washing, the structure of Co–N-CNFs showed partial collapse. In addition, their micro-porosity was highly reduced as confirmed from FE-SEM images, BET and BJH pore size distribution profiles (Fig. S7b, c, e and f, ESI†). Therefore, Co–N-CNFs after acid washing (Co–N-CNFs-acid wash) are expected to show poor charge storage performance due to lower conductivity, reduced micropores, and lower structural stability, compared to pristine Co–N-CNFs without acid washing.

Transmission electron microscopy (TEM) image of Co–N-CNFs also showed a necklace-like structure (Fig. 3d). High-magnification TEM image (Fig. 3e) showed two boundaries corresponding to N-CNFs and Co–N–C, implying the inclusion of ZIF-67 into PAN polymer fibers during the electrospinning process. Both regions contained N-doped carbon. The darker region in the case of Co–N–C was due to the presence of Co element. The presence of Co–N–C particles in N-CNFs can generate large lattice defects in the overall necklace-like Co–N-CNF carbon network, which was confirmed from the higher I_D/I_G value of Co–N-CNFs than that of N-CNFs (Fig. 2d). Elemental color mappings of Co–N-CNFs (Fig. 3f) showed the existence of C, O, N, and Co as constituents, in agreement with EDS spectra (Fig. S6c, ESI†). The presence of O element was due to surface oxidation. The existence of Co and N species was expected to enhance total charge storage efficiency due to their

pseudocapacitive contributions and enhanced electrical conductivity and wettability of electrodes.[17,45] Thus, Co–N-CNFs can be used as advanced capacitive electrode materials with improved charge storage behavior for fabricating a hybrid supercapacitor.

Surface chemical compositions and oxidation states of constituent elements present in Co–N-CNFs were examined by XPS analysis (Fig. 3g–j). The survey spectrum (Fig. 3g) of Co–N-CNFs showed the presence of C, N, Co, and O elements as constituents, consistent with EDS spectra (Fig. S6c, ESI†) and elemental color mapping analysis (Fig. 3f). Atomic percentages of C, N, O, and Co were found to be 83.63%, 8.61%, 6.3%, and 1.46%, respectively (inset of Fig. 3g). The high percentage of 'N' content originated from the decomposition of PAN (nitrile group) and ZIF-67 (imidazole group).[9,46] The high content of 'N' can not only enhance the conductivity and faradaic capacitance, but also can increase the surface wettability of the carbon material during charge–discharge cycles in the aqueous KOH electrolyte, leading to a large ECSA.[17] The deconvoluted C 1s spectrum (Fig. 3h) showed two dominant peaks at a binding energy (BE) of 284.6 eV and 285.6 eV corresponding to C–C and C–N groups, respectively, while peaks at 287.3 eV and 289.7 eV were assigned to O=C–N and O–C=O groups, respectively, indicating the presence of N element as a dopant and O element as a partially oxidized functional group.[17,46] The deconvoluted N 1s spectrum (Fig. 3i) showed five peaks with different BE values corresponding to different nitrogen configurations, namely pyridinic (398 eV), benzenoid amine (399.2 eV), pyrrole (400.4 eV), malononitrile (402.3 eV), and oxidized nitrogen (404.6 eV) species, respectively.[47] The

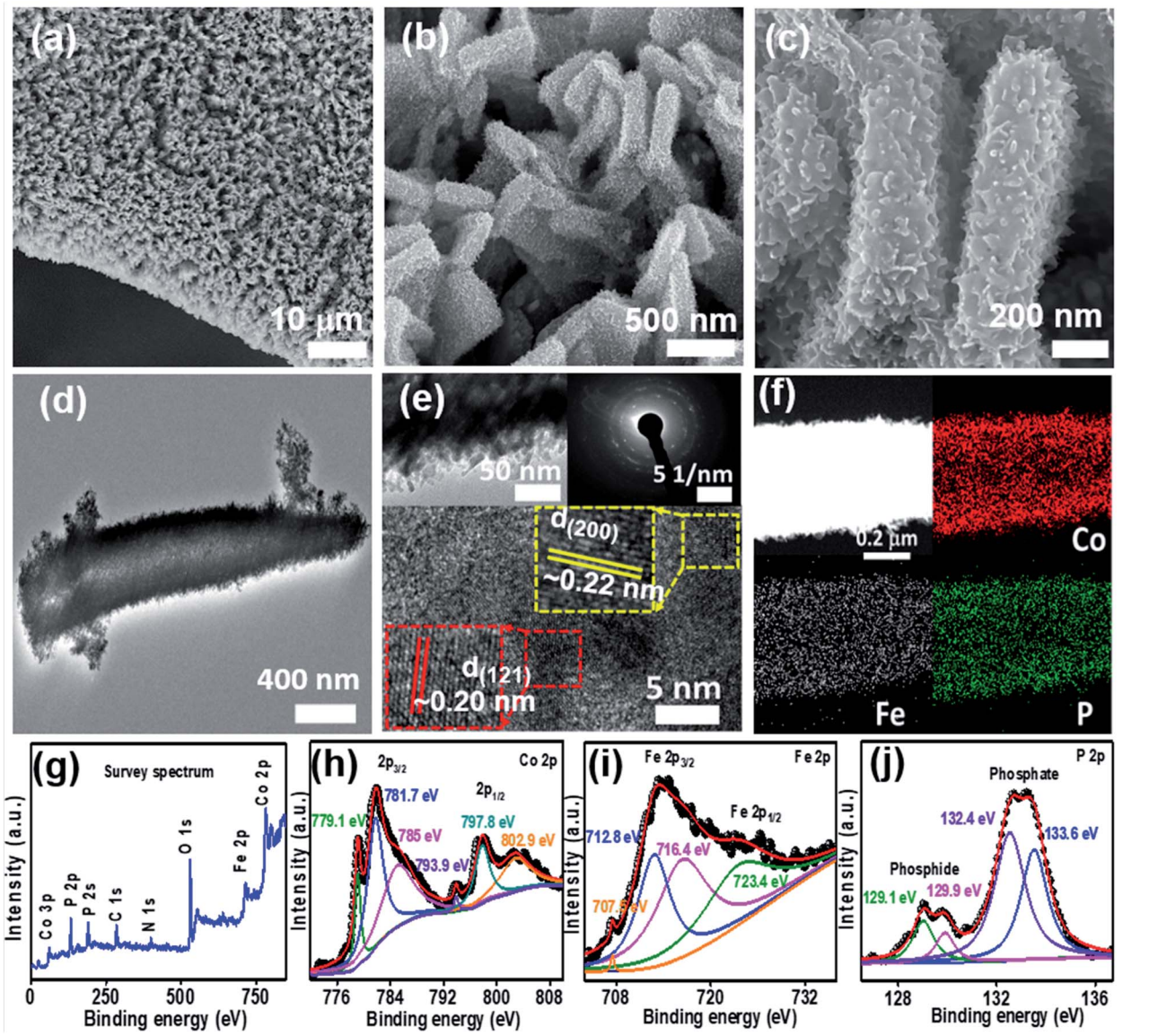

Fig. 4 (a–c) Low- and high-magnification FE-SEM images, (d and e) low- and high-magnification HR-TEM images, (f) HAADF-STEM image and EDS elemental color mapping images, (g) XPS survey spectrum, (h) Co 2p XPS spectrum, (i) Fe 2p XPS spectrum, and (j) P 2p XPS spectrum of $Co_{2-x}Fe_xP$–N–C.

deconvoluted O 1s spectrum (Fig. 3j) showed three peaks with BE values of 529.6 eV, 531.7 eV, and 534.7 eV corresponding to the M–O bond of superficially oxidized Co species, C=O, and C–O/C–OH groups, respectively.[48] The deconvoluted Co 2p spectra (Fig. S8, ESI†) showed peaks at binding energies of 778.8 eV, 780.4 eV, and 781.8 eV corresponding to metallic Co and superficially oxidized Co species due to exposure to air,[49] while the peaks at 786.1 eV and 802.7 eV are attributed to Co $2p_{3/2}$ and Co $2p_{1/2}$ satellite peaks.[49]

To further investigate the surface wettability and the conductivity of Co–N-CNFs and N-CNFs, contact angles and sheet resistances were measured using a drop shape analyser-DSA30, Kruss, and four-point-probe surface resistivity meter (Fig. S9 and Table S1, ESI†). The Co–N-CNF electrode showed a contact angle of ~61.1° and sheet resistance of 54.64 Ω sq^{-1} compared to that of N-CNFs (~146.5° and 77.42 Ω sq^{-1}). The lower value of the contact angle and the sheet resistance of Co–N-CNFs indicate its enhanced surface wettability and higher conductivity compared to N-CNFs, which can be attributed to the presence of both Co nanoparticles and N heteroatoms in the Co–N-CNF electrode.[17,35]

Likewise, the surface morphology, internal structure, surface chemical composition, and valence states of the constituent elements of the $Co_{2-x}Fe_xP$–N–C material were investigated. The results are shown in Fig. 4. The low-magnification FE-SEM image demonstrated a uniform growth of 3-D micropillar arrays of $Co_{2-x}Fe_xP$–N–C over a conductive Ni foam substrate (Fig. 4a). The high-magnification FE-SEM image (Fig. 4b) displayed empty spaces between individual micropillars that could facilitate the diffusion of electrolytes ions to reach the root of micropillar blocks. The resultant rough surface of $Co_{2-x}Fe_xP$–N–C micropillars (Fig. 4c) would be advantageous in terms of increasing the SSA over the smooth surface of pristine Co_2P–N–C (Fig. 2f and S10 in the ESI†).

HR-TEM images also showed a consistent micropillar structure with sharp nanospike-like surface defects (Fig. 4d). The magnified HR-TEM image (Fig. 4e) showed lattice fringes; the observed interplanar spacings of 0.22 nm and 0.20 nm were ascribed to (200) and (121) planes of binary phosphide phases of Fe_2P and Co_2P, respectively, consistent with PXRD results (Fig. 2c). The selected area electron diffraction (SAED) pattern (inset of Fig. 4e) showed concentric circular rings with bright distinct dots, indicating a polycrystalline nature. High angle annular dark-field scanning transmission electron microscopy (HAADF-STEM) and elemental color mappings of $Co_{2-x}Fe_xP$–N–C (Fig. 4f) showed the presence of Co, Fe, and P as the main constituents. They were uniformly distributed across the micropillar structure.

XPS analysis of $Co_{2-x}Fe_xP$–N–C are shown in Fig. 4g–j. The survey spectrum of $Co_{2-x}Fe_xP$–N–C confirmed the presence of Co, Fe, P, O, C, and N elements (Fig. 4g). The presence of C and N originated from N-doped carbon (N–C) formed under thermal decomposition of the CoFe-PBA precursor in an inert atmosphere, while the existence of O was due to partial surface oxidation.[28] The presence of N–C was expected to enhance the electrode's charge storage kinetics due to its fast EDLC nature.[3,6,7] Fig. 4h shows the splitting of the Co 2p spectrum into Co $2p_{3/2}$ and Co $2p_{1/2}$ doublets due to the spin–orbit coupling.[27,50] The deconvoluted Co $2p_{3/2}$ XPS spectrum showed three peaks at BE values of 779.1 eV, 781.7 eV, and 785 eV respectively. Peaks at 779.1 eV and 129.9 eV were very close to binding energies of Co and P species in Co_2P.[50,51] Peaks at 781.7 eV and approximately 132.4–133.6 eV corresponded to superficial oxidation of Co_2P.[50] The peak at the binding energy of 785 eV corresponded to characteristic satellite peaks of Co $2p_{3/2}$ in the Co 2p spectrum.[50] Fig. 4i shows the deconvoluted XPS spectra of the Fe 2p spectrum with peaks at BE of 712.8 eV and 723.4 eV attributed to Fe $2p_{3/2}$ and Fe $2p_{1/2}$ electronic configurations of Fe_2P, respectively.[52] Peaks at BE of 716.4 eV indicated satellite peaks of Fe^{2+} in Fe_2P,[37,50,53] while the peak at 707.5 eV was ascribed to the lower oxidation state of Fe ($Fe^{\delta+}$), which was balanced with a low-coordinated metal-phosphide structure.[50,53] The deconvoluted P 2p XPS spectrum (Fig. 4j) showed two peaks with BE values of 129.1 eV and 129.9 eV corresponding to spin–orbit peaks of P $2p_{3/2}$ and P $2p_{1/2}$ of metal phosphides, respectively, while peaks with BE values of ~132 eV and ~133 eV corresponded to oxidized PO^- species resulting from surface oxidation.[27,37,50] Thus, the phase, structure, morphology, internal structures, composition, and chemical states of the constituents and elements of $Co_{2-x}Fe_xP$–N–C/NF and Co–N-CNF electrode materials were examined by various physical characterization techniques.

3.2 Electrochemical study

3.2.1 Single electrode (negative electrode) charge storage performance of Co–N-CNFs. Initially, charge storage performances of carbonized EP-NFs (N-CNFs) and carbonized EPZ-67-NFs (Co–N-CNFs) prepared with different ratios (1 : 10, 1 : 5, and 1 : 3) of ZIF-67 to PAN were evaluated in a three-electrode configuration cell using 6 M KOH as the electrolyte. CV curves of all materials were recorded at a scan rate of 50 mV s^{-1}. Results are shown in Fig. S11a, ESI,† revealing a typical quasi-rectangular shape which indicated the EDLC nature with a partial pseudocapacitive component. Deviation from a perfect rectangular shape was due to the presence of pseudocapacitive N and O species.[9,46] Redox current and area under the CV curve were higher for Co–N-CNF materials than for N-CNFs, and their values increased with the increase of ZIF-67 loading. The optimized Co–N-CNF electrode prepared with a ZIF-67 to PAN ratio of 1 : 3 had the highest redox current, signifying higher charge storage capability. However, after acid washing, the current was drastically reduced, possibly due to the elimination of Co moieties and change in the internal pore structure (Fig. S7, ESI†). The charge and discharge times were higher for optimized Co–N-CNFs and it followed the same trend shown in CV observations. This could be due to the lower equivalent series resistance (ESR) of optimized Co–N-CNFs than other Co–N-CNF materials as shown in the Nyquist plot (Fig. S11c, ESI†). The low electrochemical performance of Co–N-CNFs (acid wash) compared to Co–N-CNFs (without acid wash) indicated that acid washing employed for creating high SSA and large pores might be unnecessary as the electrode could be used directly without acid washing to get higher performance.

After finding that the optimized Co–N-CNF electrode exhibited higher charge storage performance based on preliminary electrochemical tests, the optimized Co–N-CNF electrode was subjected to various electrochemical characterizations (Fig. 5) to know its efficiency and durability. Fig. 5a shows CV curves of the Co–N-CNF electrode recorded at different scan rates ranging from 5 to 300 mV s^{-1}. The quasi-rectangular shape was maintained even at a very high scan rate of 300 mV s^{-1}, indicating its excellent rate capability.[9,44] Fig. 5b shows a schematic model of distinct possible electrode–electrolyte interactions that can occur on a heteroatom-doped, surface oxidized carbon-based electrode material at various potentials.[9] CV profiles of the Co–N-CNF electrode with oxygen functional groups on the surface can be divided into three potential regions indicated as (1), (2), and (3) based on distinct possible electrode–electrolyte interactions (Fig. 5c). The schematic model explains three different potential regions of the CV curve (Fig. 5c) such as (1) low V, (2) medium V, and (3) high V. In the low potential region (1), hydrated potassium ions rapidly migrate toward the electrode's surface and form an outer Helmholtz layer (OHP) (Fig. 5b and c).[9] In the mid-potential region (2), hydrated potassium ions become dissipated as the interfacial tension becomes the maximum due to the steric hindrance effect arising from oxygen species on the electrode's surface and diffusion of ions into the bulk electrolyte solution becomes prominent (Fig. 5b and c).[9] Hydrated ions in the high potential region (3) are likely to be squeezed inside pores and undergo a quasi-reversible process of insertion and de-insertion of hydrated potassium ions, which adds additional capacitance (Fig. 5b and c).[9] The plausible quasi-reversible process in alkaline KOH medium is represented by eqn (10):[9]

$$A - C_xO + \left[K(H_2O)_n\right]^+ + e^- \xleftrightarrow{\text{charge/discharge}} A - C_xOK(H_2O)_{n-y} \quad (10)$$

where '*A*' represents the surface of the Co–N-CNF electrode material, '*n*' denotes the number of H_2O molecules

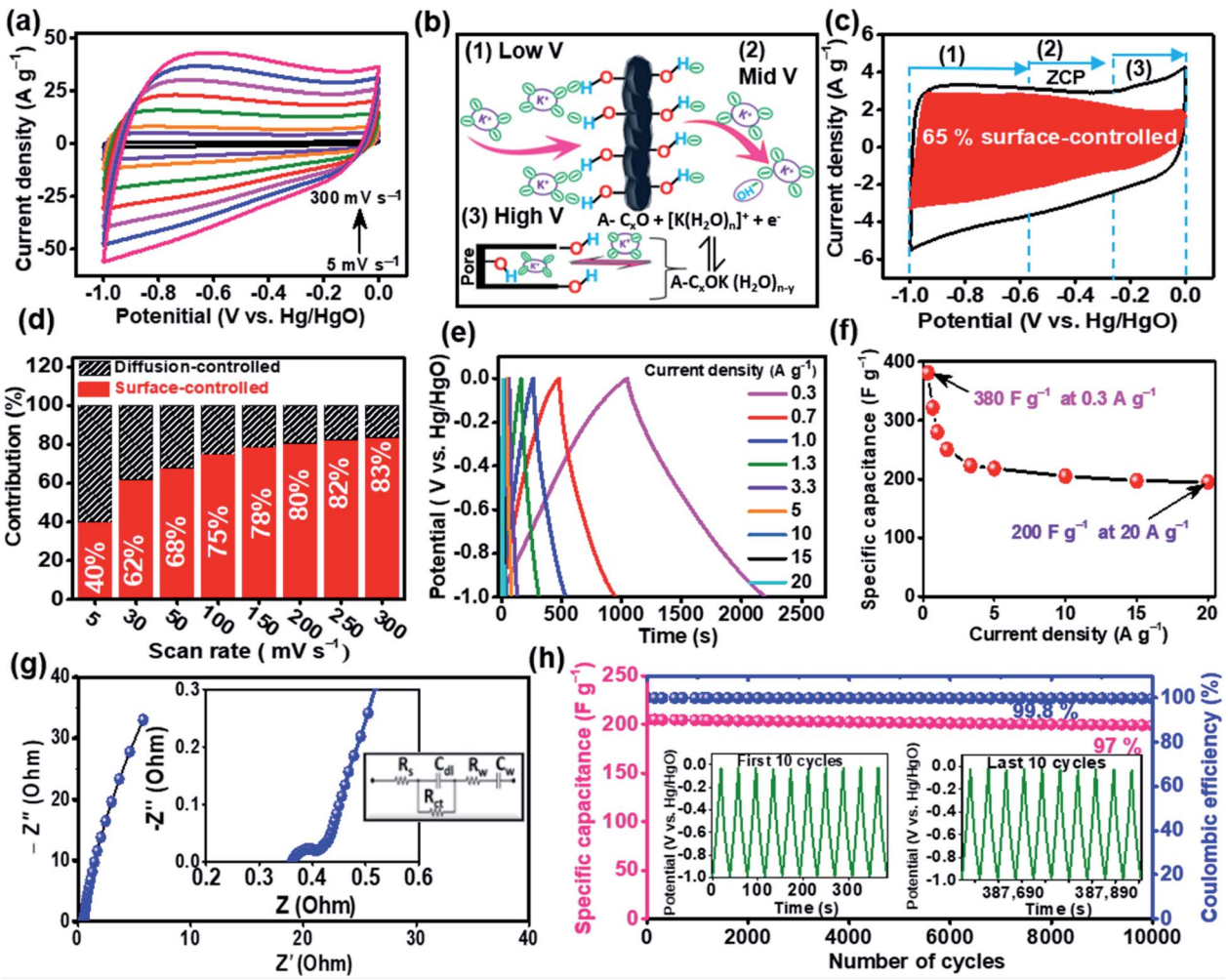

Fig. 5 Three-electrode electrochemical measurements of the Co–N-CNF negative electrode recorded in 6 M KOH electrolyte: (a) CV profiles, (b) plausible schematic representation of the formation of EDL on Co–N-CNF surfaces based on the CV curve, (c) surface-controlled contribution profile, evaluated from the CV curve (scan rate: 10 mV s^{-1}), (d) scan rate dependent surface-controlled contributions (estimated at 0.5 V *vs.* Hg/HgO) for cathodic sweeps, (e) GCD profiles, (f) comparison of specific capacitance at different current densities, (g) Nyquist plot recorded at OCP, and (h) specific capacitance retention and coulombic efficiency profiles at a current density of 10 A g^{-1} after 10 000 GCD cycles.

coordinating with potassium ion (K^+), while 'y' denotes the number of H_2O molecules lost from hydrated potassium ions under squeezing.[9]

In addition, the nature of the charge storage process was analyzed from current and scan rate relationship using the power law as shown in eqn (11):[24,54]

$$i = av^b \quad (11)$$

where 'i' is the current, 'v' is the scan rate, 'a' and 'b' are constants of fitting parameters. The 'b' value can be obtained by calculating the slope of the log(i) *vs.* log(v) curve. If the 'b' value is close to 0.5, it indicates a diffusion-controlled process.[7] If it is close to '1', it indicates a surface-controlled process that includes both pure capacitive as well as pseudocapacitive processes.[7] To estimate their contribution to total charge storage, the slope (b) of log(i) *vs.* log(v) graph was calculated at different potentials, as shown in Fig. S12a and b, ESI.† Estimated 'b' values at different potentials were between '0.5' and '1' (Fig. S12b, ESI†), showing that the charge storage was controlled by both diffusion-controlled process and surface-controlled process. The surface-controlled part can be quantified in the CV curve by deconvoluting from the total current response at a fixed potential (U) using eqn (12). The surface-controlled part is proportional to the scan rate v and the diffusion-controlled part is proportional to $v^{1/2}$ according to eqn (12):[24,54]

$$i(U) = k_1 v + k_2 v^{1/2} \quad (12)$$

where v is the scan rate and k_1 and k_2 are constants. Dividing the above equation on both sides by $v^{1/2}$, eqn (13) is obtained:

$$\frac{i\,(U)}{v^{\frac{1}{2}}} = k_1 v^{1/2} + k_2 \quad (13)$$

This equation is in the form of a straight line. Thus, k_1 and k_2 are numerically equal to the slope and y-intercept of the straight line represented by eqn (13). After obtaining k_1 and k_2 at a particular potential, the contribution of each component ($k_1 v$ giving the surface-controlled part and $k_2 v^{1/2}$ giving the diffusion-controlled part) can be easily quantified.[24,54] To deconvolute the surface-controlled part from the total charge storage of Co–N-CNFs, values of k_1 and k_2 were determined at various potentials at various scan rates (Fig. S12c, ESI†). The sum of surface-controlled parts estimated at various potentials at a fixed scan rate of 10 mV s^{-1} was found to be *ca.* 65% of total charge storage (Fig. 5c). Surface-controlled contributions at a fixed potential (−0.5 V *vs.* Hg/HgO) for cathodic sweeps at various scan rates of 5, 30, 50, 100, 150, 200, 250, and 300 mV s^{-1} were 40%, 62%, 68%, 75%, 78%, 80%, 82%, and 83%, respectively (Fig. 5d). The surface-controlled part increased with increasing scan rate while the contribution of the diffusion-controlled processes decreased. The decrease in the diffusion-controlled part could be ascribed to a decrease in the time available for the diffusion of ions into the electrode material with an increasing scan rate.[11,24] Thus, Fig. 5d clearly shows that surface-controlled contribution was more at all scan rates. These observations were consistent with previous reports.[9,11,24]

Fig. 5e shows GCD curves recorded at various current densities ranging from 0.3 A g^{-1} to 20 A g^{-1}. A typical quasi-triangular shape was found at all current densities, indicating the EDLC and pseudocapacitive nature.[3,9,17,45,55,56] The details of the calculation of galvanostatic specific capacitance values of the Co–N-CNF electrode using eqn (2) at various current densities and their values are shown in Table S2, ESI† and Fig. 5f. Specific capacitance values at 0.3 and 20 A g^{-1} were calculated to be 380 and 200 F g^{-1}, respectively. These values were much higher than those of previous reports (Table S4, ESI†). When current density was increased to 20 A g^{-1}, specific capacitance retention was 45%. A sharp decay in specific capacitance was observed only when the current density was below 4 A g^{-1}. There was no significant decay in specific capacitance for regions with high current densities (Fig. 5f), indicating the excellent charge storage and rate capability of Co–N-CNFs as an electrode material. For comparison, the voltammetric specific capacitance of the Co–N-CNF electrode was also evaluated from the corresponding CV curves (Fig. 5a) using eqn (3), and the results are shown in Fig. S13, ESI.† Co–N-CNFs showed a high specific capacitance of 393 F g^{-1} at the scan rate of 5 mV s^{-1}. Even at a high scan rate of 300 mV s^{-1}, it still demonstrated a specific capacitance of 209 F g^{-1}, which is 53.2% specific capacitance retention. Fig. 5g shows the Nyquist plot of optimized Co–N-CNFs. Generally, a Nyquist plot consists of three main characteristic regions: (i) a semi-circular region at high frequency which corresponds to the resistance of pseudo-charge-transfer processes, (ii) a mid-frequency region corresponding to Warburg impedance (W), and (iii) a vertical line along the y-axis (imaginary axis) at a low frequency which corresponds to the capacitive behavior of the electrode.[9,45,57] As observed in the inset of Fig. 5g, and S11c, ESI,† the Nyquist plot of Co–N-CNFs showed a very small semi-circular region and a nearly vertical tail, indicating a low charge transfer resistance and a dominant capacitive nature.[45,57] The equivalent circuit diagram corresponding to the Nyquist plot of Co–N-CNFs is shown in the inset of Fig. 5g in agreement with that of hetero-atom doped carbon-based materials.[9,57]

Long-term stability of the Co–N-CNF electrode is an important factor for practical applications. Therefore, 10 000 GCD cycles were carried out at a high current density of 10 A g^{-1}. The first and the last 10 GCD cycles of stability tests are shown in the inset of Fig. 5h. It was revealed that the triangular shape was maintained even at the end of 10 000 GCD cycles. The Co–N-CNF electrode exhibited excellent specific capacitance retention of 97% with a coulombic efficiency of 99.8% after 10 000 GCD cycles at very high current density (Fig. 5h). To understand the charge storage performance of the Co–N-CNF electrode compared to other carbon-based electrode materials, the specific capacitance, specific capacitance retention, and coulombic efficiency values of various materials were compared. Results are shown in Table S4, ESI.† The excellent charge storage capability and long-term stability of the Co–N-CNF electrode were attributed to its unique compositional and structural properties. (i) The combined effect of high SSA

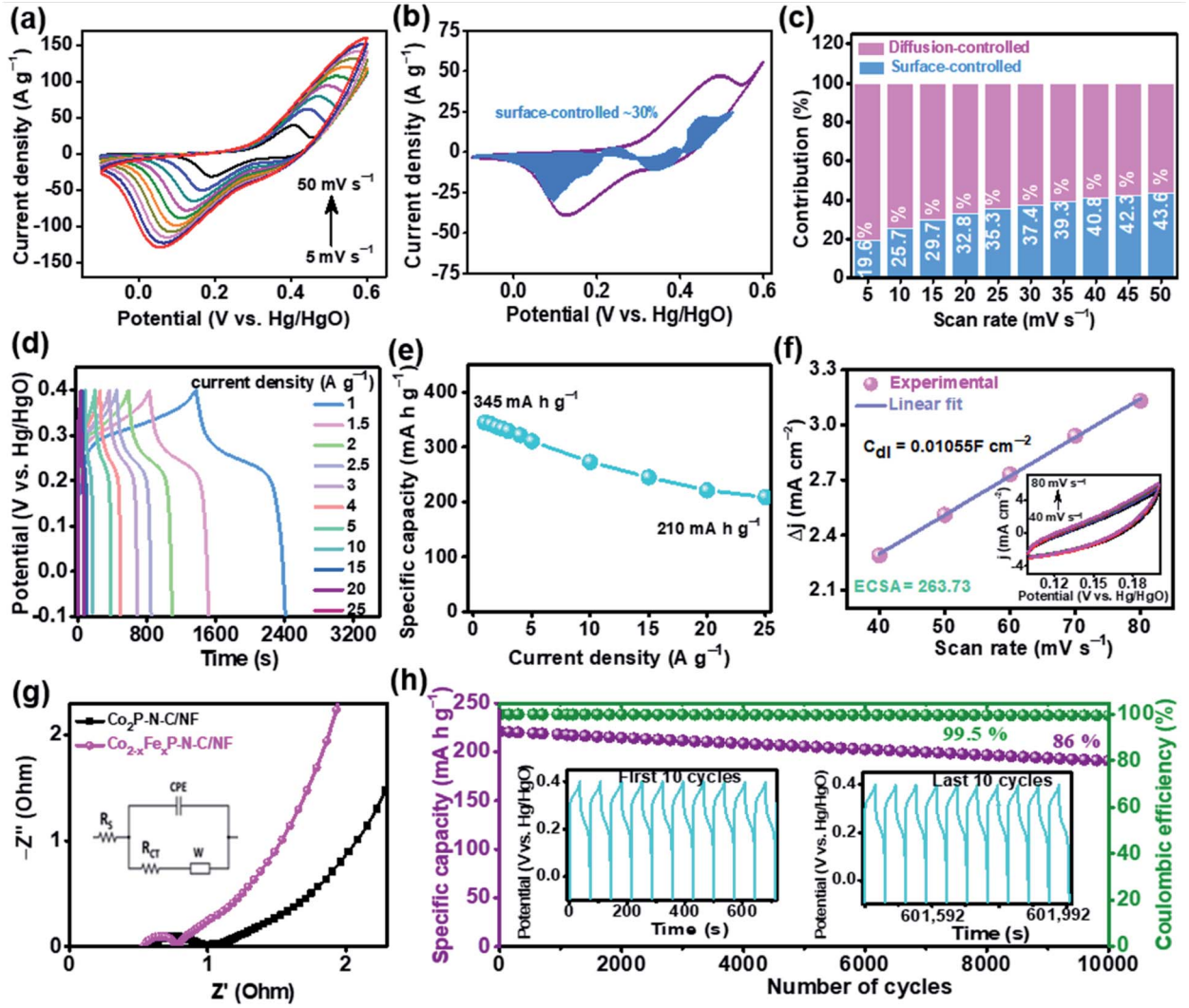

Fig. 6 Three-electrode electrochemical measurements of the $Co_{2-x}Fe_xP$–N–C/N–F positive electrode recorded in 6 M KOH electrolyte: (a) CV profiles, (b) surface-controlled contribution profile evaluated from the CV curve (scan rate: 10 mV s^{-1}), (c) scan rate dependent surface-controlled contributions at a fixed potential (0.35 V *vs.* Hg/HgO) for cathodic sweeps, (d) GCD profiles, (e) comparison of specific capacities at different current densities, (f) scan rate dependent current densities for estimating ECSA, the inset of (f) shows CV curves at various scan rates ranging from 40 to 80 mV s^{-1}, (g) Nyquist plot recorded at OCP, and (h) specific capacity retention and coulombic efficiency profiles at a current density of 20 A g^{-1}.

and the highly porous structure of Co–N-CNFs ensured excellent ion/electron movements. High micro-porosity also enhances the capacitance *via* the "nano-confinement effect".[9,41,42,44,58,59] (ii) The presence of metallic Co nanoparticles and N-doping originating from the decomposition of organic components enhanced the electrical conductivity and pseudo-capacitance which contributed to the total capacitance.[9,46,55] (iii) The presence of N atoms and oxygen-containing functional groups on the carbon surface improved the wettability of the electrode, thereby improving the ion migration rate and lowering the mass transfer resistance and also contributes to the total charge storage due to their pseudocapacitive nature.[9,16,45] Owing to such high charge storage performance, Co–N-CNFs can serve as excellent negative electrode materials for the fabrication of hybrid supercapacitors.

3.2.2 Single electrode (positive electrode) charge storage performance of $Co_{2-x}Fe_xP$–N–C/NF. Besides the high performance of the capacitive negative electrode material, it is equally important to have high charge storage capability of the counterpart battery-type positive electrode for making an efficient hybrid supercapacitor. Therefore, the charge storage performance of the synthesized $Co_{2-x}Fe_xP$–N–C/NF (positive electrode) was also evaluated in a three-electrode configuration cell using 6 M KOH as the electrolyte (Fig. 6). Fig. 6a shows CV curves of the mesoporous $Co_{2-x}Fe_xP$–N–C/NF electrode recorded at various scan rates ranging from 5 to 50 mV s^{-1}. At all scan rates, CV curves exhibit redox peaks resulting from the oxidation and reduction processes, indicating the faradaic nature and battery-type charge storage characteristics.[3,23,55] Since there was a small amount of N–C in the synthesized $Co_{2-x}Fe_xP$–N–C/

NF micropillar structure, N–C species were expected to contribute to total charge storage due to their capacitive nature. Thus, diffusion-controlled and surface-controlled contributions of the $Co_{2-x}Fe_xP$–N–C/NF electrode to the total charge stored were evaluated in the same manner as that of the Co–N-CNF electrode. The '*b*' values were obtained by calculating the slope of the log(*i*) *vs.* log(*v*) curves, as shown in Fig. S14a.† The obtained '*b*' values were between 0.5 and 1, but closer to 0.5 (Fig. S14b†), which indicated that the diffusion-controlled part was dominant compared to the surface-controlled part in the total charge storage. The surface-controlled part (k_1v) and diffusion-controlled part ($k_2v^{1/2}$) in the total charge storage of $Co_{2-x}Fe_xP$–N–C/NF were determined after finding the values of k_1 and k_2 at various potentials under various scan rates (Fig. S14c, ESI†). The results are shown in Fig. 6b and c. At a fixed scan rate of 10 mV s^{-1}, the surface-controlled contribution to the total charge was 30% (Fig. 6b). Surface-controlled contributions to total charge storage at a fixed potential (0.35 V *vs.* Hg/HgO) for cathodic sweeps with various scan rates of 5, 10, 15, 20, 25, 30, 35, 40, 45, and 50 mV s^{-1} were 19.6%, 25.7%, 29.7%, 32.8%, 35.3%, 37.4%, 39.3%, 40.8%, 42.3%, and 43.6%, respectively (Fig. 6c). Such surface-controlled contributions to the total charge storage of the $Co_{2-x}Fe_xP$–N–C/NF electrode were expected from N-doped carbon species originating from the thermal decomposition of CoFe-PBA in an Ar atmosphere.[28] However, such surface-controlled contribution was relatively lower than the contribution of the diffusion-controlled part at all scan rates (Fig. 6c). This signifies that charge-storage is mainly from the diffusion-controlled process, demonstrating the nature of a battery-type electrode.[24,55] To quantify the capacity of the electrode, a number of galvanostatic charge–discharge (GCD) measurements were performed at various current densities ranging from 1 to 25 A g^{-1} (Fig. 6d). GCD curves (Fig. 6d) showed clear plateau regions between ~0.3 and ~0.2 V, indicating the nature of a battery-type electrode, consistent with CV observations. The details of the calculation of the specific capacities of the $Co_{2-x}Fe_xP$–N–C/NF electrode at different current densities using eqn (4) and their values are shown in Table S3, ESI† and Fig. 5e. The $Co_{2-x}Fe_xP$–N–C/NF electrode exhibited specific capacities of 345, 337, 330, 322, 311, 273, 245, 221, and 210 mA h g^{-1} at current densities of 1, 2, 3, 4, 5, 10, 15, 20, and 25 A g^{-1} respectively. The $Co_{2-x}Fe_xP$–N–C/NF electrode retained 60.8% of specific capacity even at a very high current density of 25 A g^{-1} indicating its excellent rate capability.[60] The calculated specific capacity values of the $Co_{2-x}Fe_xP$–N–C/NF electrode were much higher than those of other materials recently reported (Table S5†). To find an accessible electrode surface for electrolyte ions, electrochemically active surface area (ECSA) was evaluated using eqn (5). The calculated ECSA of the $Co_{2-x}Fe_xP$–N–C/NF electrode material was as high as 263.73 (Fig. 6f), indicating that the porous micropillar morphology with enormous surface defects could provide abundant redox active sites.[23,24,37] Fig. 6g shows Nyquist plots of $Co_{2-x}Fe_xP$–N–C/NF and Co-MOF/NF-derived Co_2P–N–C/NF. The smaller semi-circular portion of $Co_{2-x}Fe_xP$–N–C/NF compared to Co_2P–N–C/NF in the high-frequency region indicated a low ESR.[61] CV and GCD profiles of $Co_{2-x}Fe_xP$–N–C/NF were also compared with those of the pristine Co_2P–N–C/NF electrode material to check the influence of Fe in the $Co_{2-x}Fe_xP$–N–C/NF composite (Fig. S15, ESI†). Results showed a much higher performance of $Co_{2-x}Fe_xP$–N–C/NF compared to Co_2P–N–C/NF due to enhanced conductivity. Besides, the stability of the electrode can be evaluated more precisely from long-term cycling at high current densities. Therefore, the $Co_{2-x}Fe_xP$–N–C/NF electrode material was subjected to 10 000 continuous GCD cycles at a high current density of 20 A g^{-1} (Fig. 6h). The inset of Fig. 6h shows the first 10 and the last 10 GCD cycles of 10 000 GCD cycles. Shapes of curves are maintained even after long-term stability. After 10 000 GCD cycles, the specific capacity of the electrode was only reduced by 14% compared to the initial value, and it had a coulombic efficiency of 99.5%, indicating its excellent robustness and reversibility.[23] Thus, CV, GCD, and EIS analysis results confirmed that $Co_{2-x}Fe_xP$–N–C/NF would be an excellent battery type positive electrode material for fabricating a hybrid supercapacitor. The charge storage performance of the $Co_{2-x}Fe_xP$–N–C/NF electrode was also compared with various recently reported battery-type electrode materials (Table S5, ESI†). Results indicated that our $Co_{2-x}Fe_xP$–N–C/NF electrode material was much superior in terms of specific capacity and cycling stability (Table S5, ESI†). Such an excellent performance of $Co_{2-x}Fe_xP$–N–C/NF electrode materials is attributed to its unique compositional, structural, and morphological features due to the following reasons: (i) the synergistic effect of Co, Fe, and P ions (Co provides high capacity while Fe and P provide high conductivity),[23,24] (ii) direct growth of $Co_{2-x}Fe_xP$–N–C micropillar arrays on the Ni foam substrate avoids the usage of polymer binders and conductive additives, thereby significantly reducing the inactive "dead volume,[23,24,27,37,59] (iii) the 3-D electrode architecture enhances the interfacial contact between the active $Co_{2-x}Fe_xP$–N–C material and the Ni foam substrate, thereby remarkably enhancing ion transportation while also providing an effective pathway for high electron transport during the cycling, resulting in exceptional cycle stability,[27,37,59] (iv) the large SSA and highly porous structure resulting from high surface defects of the 3-D $Co_{2-x}Fe_xP$–N–C micropillar arrays could largely enhance ECSA, thus boosting the charge storage performance,[23,24,27,37] and (v) the presence of trace amount of N–C can also improve the charge-storage kinetics of the $Co_{2-x}Fe_xP$–N–C/NF electrode.[27,28] The effect of using Ni foam as a substrate and current collector was also investigated by evaluating its CV curve in the same potential window of the positive as well as the negative electrode materials under the same electrochemical setup and the conditions. The CV profiles of bare Ni foam at the scan rate of 10 mV s^{-1} compared with those of Co–N-CNFs and $Co_{2-x}Fe_xP$–N–C/NF showed its negligible contribution (Fig. S16, ESI†), implying that the high electrochemical charge storage performances were resulted solely from the active electrode materials.

3.2.3 Fabrication of $Co_{2-x}Fe_xP$–N–C/NF(+)//Co–N-CNFs(−) solid-state hybrid supercapacitor (SSHSC) and its charge storage performance. To demonstrate the suitability of the synthesized electrode materials for practical applications, we assembled a solid-state hybrid supercapacitor (SSHSC) using

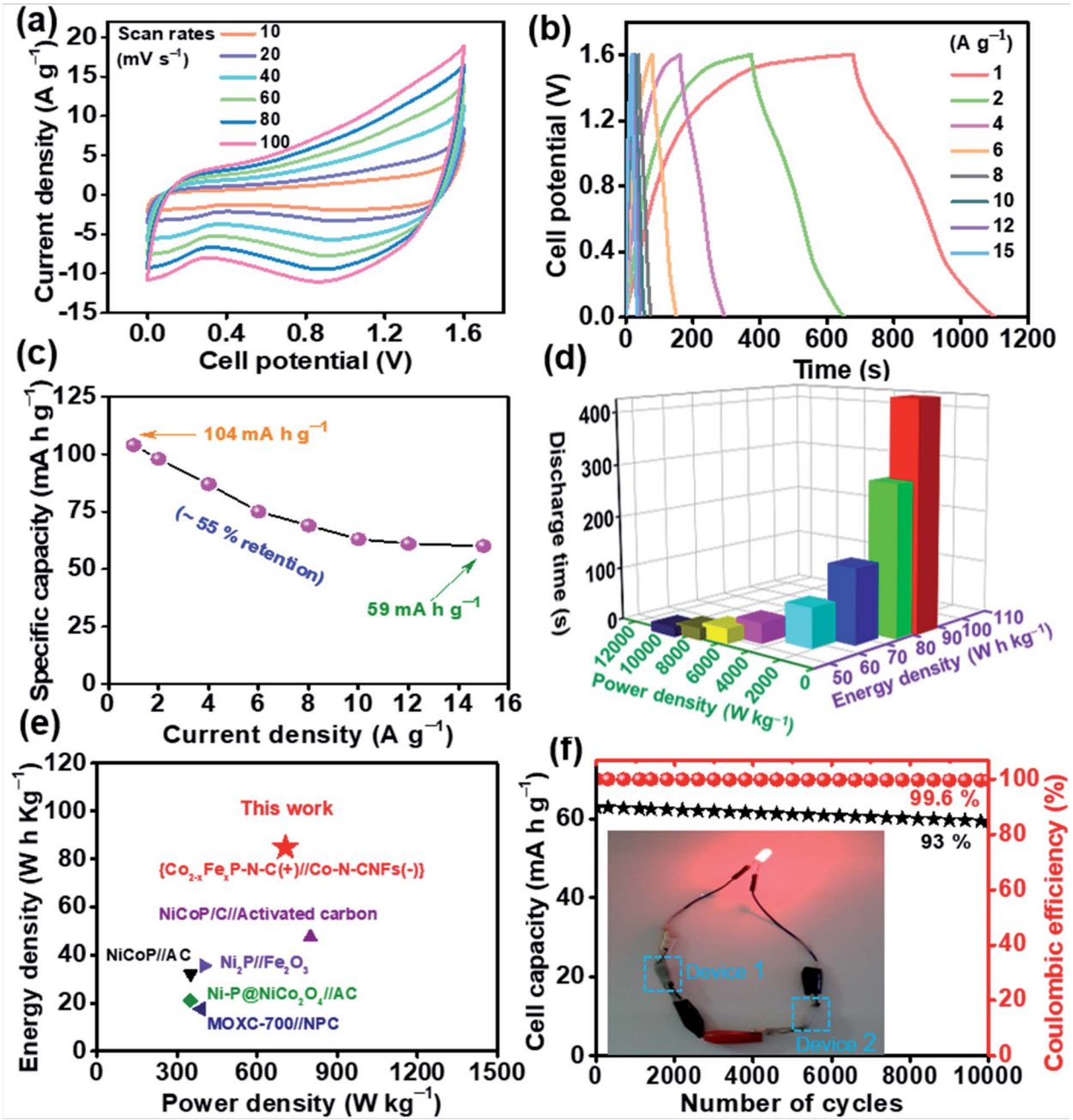

Fig. 7 Electrochemical study of the $Co_{2-x}Fe_xP$–N–C/N–F/(PVA/KOH)/Co–N-CNF solid-state hybrid supercapacitor device: (a) CV profiles, (b) GCD profiles, (c) comparison of specific capacities at different current densities, (d) Ragone plot (power density *vs.* energy density), (e) energy and power density compared to those of recently reported hybrid supercapacitor devices: NiCoP/C//activated carbon,[62] MOXC-700//NPC,[63] Ni_2P//Fe_2O_3,[64] NiCoP//AC,[65] NiP@$NiCo_2O_4$//AC,[66] (f) cycling stability and coulombic efficiency at 10 A g^{-1} (inset shows the glowing of LED bulb with two identical hybrid supercapacitors connected in series).

Co–N-CNFs and $Co_{2-x}Fe_xP$–N–C/NF as negative (capacitive) and positive (faradaic battery-type) electrodes, respectively. These two electrodes were sandwiched with a cellulose paper and solid-state gel electrolyte (KOH/poly(vinyl alcohol) (PVA)). The entire setup assembled in a split test cell is shown in Fig. S17a, ESI.† Fig. S17b in the ESI† shows three-electrode CV curves of Co–N-CNFs and $Co_{2-x}Fe_xP$–N–C/NF electrodes. Both the CV profiles indicated that the SSHSC was made with electrodes having capacitive and battery-type electrode nature.[3,6,55] To choose the potential window for SSHSC, we recorded CVs in different potential windows as shown in Fig. S17c, ESI.† From these observations, we found that 1.6 V was a suitable potential window for electrochemical evaluation because, after 1.6 V, oxidation current started to increase sharply due to the association of various other electrochemical processes. Fig. 7a shows CV curves of the $Co_{2-x}Fe_xP$–N–C/NF(+)//Co–N-CNFs(−) SSHSC

recorded at different scan rates ranging from 10 to 100 mV s^{-1} with a potential window of 1.6 V. The typical CV shape of the SSHSC device at all scan rates demonstrated mixed charge storage characteristics (EDLC and faradaic).[3,6,55] Fig. 7b shows GCD profiles of the SSHSC device recorded at various current densities ranging from 1 to 15 A g^{-1} with a potential window of 1.6 V. GCD curves of the SSHSC device also showed mixed/hybrid capacitive characteristics, consistent with CV observations. From the discharge portion of GCD curves, specific capacities of the hybrid device at various current densities were calculated using eqn (6). The results are presented in Fig. 7c. The SSHSC device exhibited high specific capacities of 104 mA h g^{-1} and 59 mA h g^{-1} at a current density of 1 and 15 A g^{-1}, respectively. The SSHSC device retained 55% of its specific capacity even at a high current density of 15 A g^{-1} (Fig. 7c). Both energy and power densities are very important parameters to assess the performance of any supercapacitor device. Therefore, energy and power densities of the hybrid supercapacitor device were calculated using eqn (8) and (9). The results are shown in Fig. 7d. Our SSHSC device demonstrated a high energy density of 84.7 W h kg^{-1} at a power density of 706 W kg^{-1}. Even at the high power density of 9200 W kg^{-1}, it demonstrated a remarkably high energy density of 46 W h kg^{-1}. This is a quite promising result. Ragone plot (Fig. 7e) was also made to show the high energy and power densities of our $Co_{2-x}Fe_xP$–N–C/NF(+)//Co–N-CNFs(−) SSHSC device compared to the very recently reported asymmetric/hybrid supercapacitor devices prepared with different electrode materials.

Ragone plot (Fig. 7e) showed high energy and power density values for the $Co_{2-x}Fe_xP$–N–C/NF(+)//Co–N-CNFs(−) SSHSC device compared to other asymmetric/hybrid supercapacitor devices such as NiCoP/C//activated carbon,[62] MOXC-700//NPC,[63] Ni_2P//Fe_2O_3,[64] NiCoP//AC,[65] and NiP@$NiCo_2O_4$//AC,[66] and so on. Besides the excellent specific capacity, energy density, and power density, the long-term stability of the device is also essential for practical application. Therefore, 10 000 GCD cycles were carried out continuously at a constant high current density of 10 A g^{-1} (Fig. 7f). Interestingly, the fabricated $Co_{2-x}Fe_xP$–N–C/NF(+)//Co–N-CNFs(−) SSHSC device showed high capacity retention of 93% even after 10 000 GCD cycles, indicating its excellent stability under long-term cycling test. The coulombic efficiency of the SSHSC device was 99.6% after 10 000 GCD cycles (Fig. 7f), signifying its excellent reversibility. To show its high charge storage performance, two identical SSHSCs connected in series were then connected to an LED red bulb. It effectively lighted the LED bulb, as shown in the inset of Fig. 7f. This signifies the potential applicability of the assembled SSHSC for various purposes. High energy density, power density, and excellent stability of the $Co_{2-x}Fe_xP$–N–C/NF(+)//Co–N-CNFs(−) SSHSC were achieved due to the synergistic effect between $Co_{2-x}Fe_xP$–N–C/NF positive and Co–N-CNFs negative electrodes. The charge storage performance of the $Co_{2-x}Fe_xP$–N–C/NF(+)//Co–N-CNFs(−) SSHSC was compared to various other recently reported devices (Table S6, ESI†) which showed its superiority in terms of energy density, power density, and cycling stability. Electrochemical results confirmed that Co–N-CNFs and $Co_{2-x}Fe_xP$–N–C/NF electrodes could effectively boost the performance of the SSHSC. Thus, it is highly promising for developing high energy density and power density supercapacitors with excellent cycling stability, suggesting the effectiveness of the developed electrode materials and employed synthesis routes.

4. Conclusion

In summary, a new material of multi-component and optimized Co–N-CNF material derived from ZIF-67 (MOF) and PAN NFs was successfully fabricated. It demonstrated excellent physicochemical properties such as large SSA, high porosity, and high conductivity. It showed EDLC and pseudocapacitive characteristics due to the presence of C, N, O, and Co elements. The Co–N-CNF electrode exhibited high specific capacitance, with excellent stability and reversibility. $Co_{2-x}Fe_xP$–N–C/NF micropillars derived from CoFe-PBA/NF also showed robust architectures with high porosity, large SSA, and high conductivity compared to metal phosphides synthesized from direct methods and pristine Co_2P–N–C/NF. Using Co–N-CNFs as the negative electrode, $Co_{2-x}Fe_xP$–N–C/NF as the positive electrode, and PVA/KOH gel as the electrolyte, a solid-state hybrid supercapacitor was fabricated. This SSHSC exhibited an energy density of 84.7 W h kg^{-1} at a power density of 706 W kg^{-1} with excellent cycling stability and reversibility up to 10 000 GCD cycles at a high current density of 10 A g^{-1}. Our work highlights the importance of using MOF-based materials to obtain highly efficient multi-component hybrid electrodes with improved charge storage characteristics. Due to the excellent redox behavior of cobalt, its presence in the positive and negative electrode materials boosted the overall performance of the SSHSC. Moreover, the synthesis procedures adopted in this study and the precursor materials used are simple and economical. They can be easily scaled up and extended to synthesize other MOF-based electrode materials. It can be concluded that Co–N-CNFs and $Co_{2-x}Fe_xP$–N–C/NF have extensive potential for use in low-cost and efficient solid-state hybrid supercapacitors as well as other energy storage devices.

Conflicts of interest

There are no conflicts to declare.

Acknowledgements

This study was supported by the Nano-Material Technology Development Program (NRF-2016M3A7B4900117), the Regional Leading Research Center Program (2019R1A5A8080326), and the Program for Fostering Next Generation Researchers in Engineering (2017H1D8A2030449) through the National Research Foundation (NRF) of Korea funded by the Ministry of Science and ICT, Republic of Korea.

References

1 T. M. Gür, *Energy Environ. Sci.*, 2018, **11**, 2696–2767.

2 O. Krishan and S. Suhag, *Int. J. Energy Res.*, 2019, **43**, 6171–6210.
3 P. Simon, Y. Gogotsi and B. Dunn, *Science*, 2014, **343**, 1210–1211.
4 T. H. Ko, C. Kwak, J. Seong, Y. Cho, D. Lei, W. Choi, Y. Kuk, M. Seo and B. Kim, *Funct. Compos. Struct.*, 2019, **1**, 045003.
5 D. Kang, G. P. Ojha and H. Y. Kim, *Funct. Compos. Struct.*, 2019, **1**, 045004.
6 D. P. Dubal, O. Ayyad, V. Ruiz and P. Gómez-Romero, *Chem. Soc. Rev.*, 2015, **44**, 1777–1790.
7 Y. Wang, Y. Song and Y. Xia, *Chem. Soc. Rev.*, 2016, **45**, 5925–5950.
8 V. Barranco, M. A. Lillo-Rodenas, A. Linares-Solano, A. Oya, F. Pico, J. Ibañfez, F. Agullo-Rueda, J. M. Amarilla and J. M. Rojo, *J. Phys. Chem. C*, 2010, **114**, 10302–10307.
9 Y. He, Y. Zhang, X. Li, Z. Lv, X. Wang, Z. Liu and X. Huang, *Electrochim. Acta*, 2018, **282**, 618–625.
10 L. L. Zhang and X. S. Zhao, *Chem. Soc. Rev.*, 2009, **38**, 2520–2531.
11 T. Kshetri, D. T. Tran, T. I. Singh, N. H. Kim, K. Lau and J. H. Lee, *Compos. B Eng.*, 2019, **178**, 107500.
12 S. B. Singh, T. I. Singh, N. H. Kim and J. H. Lee, *J. Mater. Chem. A*, 2019, **7**, 10672–10683.
13 B. S. Soram, I. S. Thangjam, J. Y. Dai, T. Kshetri, N. H. Kim and J. H. Lee, *Chem. Eng. J.*, 2020, **395**, 125019.
14 U. N. Pan, V. Sharma, T. Kshetri, T. I. Singh, D. R. Paudel, N. H. Kim and J. H. Lee, *Small*, 2020, **16**, 2001691.
15 K. Kierzek, E. Frackowiak, G. Lota, G. Gryglewicz and J. Machnikowski, *Electrochim. Acta*, 2004, **49**, 515–523.
16 G. Salitra, A. Soffer, L. Eliad, Y. Cohen and D. Aurbach, *J. Electrochem. Soc.*, 2000, **147**, 2486.
17 Y. Deng, Y. Xie, K. Zou and X. Ji, *J. Mater. Chem. A*, 2016, **4**, 1129–1532.
18 B. Y. Guan, X. Y. Yu, H. Bin Wu and X. W. D. Lou, *Adv. Mater.*, 2017, **29**, 1–20.
19 L. Yu, H. Hu, H. Bin Wu and X. W. D. Lou, *Adv. Mater.*, 2017, **29**, 1604563.
20 H. Bin Wu and X. W. Lou, *Sci. Adv.*, 2017, **3**, 1–17.
21 H. Zhang, J. Nai, L. Yu and X. W. (David) Lou, *Joule*, 2017, **1**, 77–107.
22 W. Chaikittisilp, M. Hu, H. Wang, H.-S. Huang, T. Fujita, K. C.-W. Wu, L.-C. Chen, Y. Yamauchi and K. Ariga, *Chem. Commun.*, 2012, **48**, 7259.
23 X. Li, A. M. Elshahawy, C. Guan and J. Wang, *Small*, 2017, **13**, 1–24.
24 Y. Lan, H. Zhao, Y. Zong, X. Li, Y. Sun, J. Feng, Y. Wang, X. Zheng and Y. Du, *Nanoscale*, 2018, **10**, 11775–11781.
25 G. Rajeshkhanna, T. I. Singh, N. H. Kim and J. H. Lee, *ACS Appl. Mater. Interfaces*, 2018, **10**, 42453–42468.
26 G. Rajeshkhanna and G. Ranga Rao, *Electrochim. Acta*, 2018, **261**, 265–274.
27 T. I. Singh, G. Rajeshkhanna, S. B. Singh, T. Kshetri, N. H. Kim and J. H. Lee, *ChemSusChem*, 2019, **12**, 4810–4823.
28 N. Wang, W. Ma, Z. Ren, Y. Du, P. Xu and X. Han, *J. Mater. Chem. A*, 2018, **6**, 884–895.
29 N. L. Torad, R. R. Salunkhe, Y. Li, H. Hamoudi, M. Imura, Y. Sakka, C. C. Hu and Y. Yamauchi, *Chem.–Eur J.*, 2014, **20**, 7895–7900.
30 T. Kshetri, D. T. Tran, D. C. Nguyen, N. H. Kim, K. tak Lau and J. H. Lee, *Chem. Eng. J.*, 2020, **380**, 122543.
31 S. Vaquero, J. Palma, M. Anderson and R. Marcilla, *Int. J. Electrochem. Sci.*, 2013, **8**, 10293–10307.
32 L. Q. Mai, A. Minhas-Khan, X. Tian, K. M. Hercule, Y. L. Zhao, X. Lin and X. Xu, *Nat. Commun.*, 2013, **4**, 1–7.
33 C. Wei, S. Sun, D. Mandler, X. Wang, S. Z. Qiao and Z. J. Xu, *Chem. Soc. Rev.*, 2019, **48**, 2518–2534.
34 R. Banerjee, A. Phan, B. Wang, C. Knobler, H. Furukawa, M. O'Keeffe and O. M. Yaghi, *Science*, 2008, **319**, 939–943.
35 R. R. Salunkhe, Y. V. Kaneti, J. Kim, J. H. Kim and Y. Yamauchi, *Acc. Chem. Res.*, 2016, **49**, 2796–2806.
36 M. Zhi, C. Xiang, J. Li, M. Li and N. Wu, *Nanoscale*, 2013, **5**, 72–88.
37 E. Hu, J. Ning, D. Zhao, C. Xu, Y. Lin, Y. Zhong, Z. Zhang, Y. Wang and Y. Hu, *Small*, 2018, **14**, 1704233.
38 J. Bin Wu, M. L. Lin, X. Cong, H. N. Liu and P. H. Tan, *Chem. Soc. Rev.*, 2018, **47**, 1822–1873.
39 K. S. W. Sing, D. H. Everett, R. A. W. Haul, L. Moscou, R. A. Pierotti, J. Rouquerol and T. Siemieniewska, *Pure Appl. Chem.*, 1985, **57**, 603–619.
40 K. A. Cychosz, R. Guillet-Nicolas, J. García-Martínez and M. Thommes, *Chem. Soc. Rev.*, 2017, **46**, 389–414.
41 C. Prehal, C. Koczwara, N. Jäckel, A. Schreiber, M. Burian, H. Amenitsch, M. A. Hartmann, V. Presser and O. Paris, *Nat. Energy*, 2017, **2**, 16215.
42 R. Heimböckel, F. Hoffmann and M. Fröba, *Phys. Chem. Chem. Phys.*, 2019, **21**, 3122–3133.
43 C. Wang, C. Liu, J. Li, X. Sun, J. Shen, W. Han and L. Wang, *Chem. Commun.*, 2017, **53**, 1751–1754.
44 C. Wang, Y. V. Kaneti, Y. Bando, J. Lin, C. Liu, J. Li and Y. Yamauchi, *Mater. Horiz.*, 2018, **5**, 394–407.
45 H. Chen, F. Yu, G. Wang, L. Chen, B. Dai and S. Peng, *ACS Omega*, 2018, **3**, 4724–4732.
46 K. Wei, K. O. Kim, K. H. Song, C. Y. Kang, J. S. Lee, M. Gopiraman and I. S. Kim, *J. Mater. Sci. Technol.*, 2017, **33**, 424–431.
47 J. R. Pels, F. Kapteijn, J. A. Moulijn, Q. Zhu and K. M. Thomas, *Carbon*, 1995, **33**, 1641–1653.
48 G. R. Dillip, A. N. Banerjee, V. C. Anitha, B. Deva Prasad Raju, S. W. Joo and B. K. Min, *ACS Appl. Mater. Interfaces*, 2016, **8**, 5025–5039.
49 M. C. Biesinger, B. P. Payne, A. P. Grosvenor, L. W. M. Lau, A. R. Gerson and R. S. C. Smart, *Appl. Surf. Sci.*, 2011, **257**, 2717–2730.
50 P. E. R. Blanchard, A. P. Grosvenor, R. G. Cavell and A. Mar, *Chem. Mater.*, 2008, **20**, 7081–7088.
51 D. Das and K. K. Nanda, *Nano Energy*, 2016, **30**, 303–311.
52 B. Owens-Baird, Y. V. Kolen'ko and K. Kovnir, *Chem.–Eur J.*, 2018, **24**, 7298–7311.
53 C. Tang, L. Gan, R. Zhang, W. Lu, X. Jiang, A. M. Asiri, X. Sun, J. Wang and L. Chen, *Nano Lett.*, 2016, **16**, 6617–6621.

54 H. Lindström, S. Södergren, A. Solbrand, H. Rensmo, J. Hjelm, A. Hagfeldt and S. E. Lindquist, *J. Phys. Chem. B*, 1997, **101**, 7717–7722.
55 Y. Gogotsi and R. M. Penner, *ACS Nano*, 2018, **12**, 2081–2083.
56 J. Li, K. Liu, X. Gao, B. Yao, K. Huo, Y. Cheng, X. Cheng, D. Chen, B. Wang, W. Sun, D. Ding, M. Liu and L. Huang, *ACS Appl. Mater. Interfaces*, 2015, **7**, 24622–24628.
57 H. L. Girard, H. Wang, A. D'Entremont and L. Pilon, *J. Phys. Chem. C*, 2015, **119**, 11349–11361.
58 L.-F. Chen, Y. Lu, L. Yu and X. W. Lou, *Energy Environ. Sci.*, 2017, **10**, 1777–1783.
59 X. C. Xie, K. J. Huang and X. Wu, *J. Mater. Chem. A*, 2018, **6**, 6754–6771.
60 R. Wang, C. Xu and J. M. Lee, *Nano Energy*, 2016, **19**, 210–221.
61 B. A. Mei, O. Munteshari, J. Lau, B. Dunn and L. Pilon, *J. Phys. Chem. C*, 2018, **122**, 194–206.
62 Q. Zhou, Y. Gong and K. Tao, *Electrochim. Acta*, 2019, **320**, 134582.
63 A. Mahmood, R. Zou, Q. Wang, W. Xia, H. Tabassum, B. Qiu and R. Zhao, *ACS Appl. Mater. Interfaces*, 2016, **8**, 2148–2157.
64 D. Wang, L.-B. Kong, M.-C. Liu, Y.-C. Luo and L. Kang, *Chem.–Eur J.*, 2015, **21**, 17897–17903.
65 Y. M. Hu, M. C. Liu, Y. X. Hu, Q. Q. Yang, L. Bin Kong and L. Kang, *Electrochim. Acta*, 2016, **215**, 114–125.
66 X. Li, R. Ding, L. Yi, W. Shi, Q. Xu and E. Liu, *Electrochim. Acta*, 2016, **222**, 1169–1175.